

The Galaxy Populations of X-Ray Detected, Poor Groups

Kim-Vy H. Tran

Department of Astronomy & Astrophysics, University of California, Santa Cruz, CA 95064

vy@ucolick.org

Luc Simard ¹

*University of California Observatories/Lick Observatory, University of California, Santa Cruz,
CA 95064*

lsimard@as.arizona.edu

Ann I. Zabludoff ¹

*University of California Observatories/Lick Observatory, University of California, Santa Cruz,
CA 95064*

azabludoff@as.arizona.edu

John S. Mulchaey

*Observatories of the Carnegie Institution of Washington, 813 Santa Barbara St., Pasadena, CA
91101*

mulchaey@ociw.edu

ABSTRACT

We determine the quantitative morphology and star formation properties of galaxies in six nearby X-ray detected, poor groups using multi-object spectroscopy and wide-field R imaging. The mean recessional velocities of the galaxy groups range from 2843 to 7558 km s⁻¹. Each group has 15 to 38 confirmed members ranging in luminosity from dwarfs to giants ($-13.7 \geq M_R - 5\log h \geq -21.9$). We measure structural parameters for each galaxy by fitting a PSF-convolved, two component model to their surface brightness profiles. To compare directly the samples, we fade, smooth, and rebin each galaxy image so that we effectively observe each galaxy at the same redshift (9000 km s⁻¹) and physical resolution ($0.87h^{-1}$ kpc). The structural parameters are combined with [OII] measurements to test for correlations between morphological characteristics and current star formation in these galaxies. We compare results for the groups to a sample

¹Department of Astronomy and Steward Observatory, University of Arizona, Tucson, AZ 85721

of field galaxies. We find that: 1) Galaxies spanning a wide range in morphological type and luminosity are well-fit by a de Vaucouleurs bulge with exponential disk profile. 2) Morphologically classifying these nearby group galaxies by their bulge fraction (B/T) is fairly robust on average, even when their redshift has increased by up to a factor of four and the effective resolution of the images is degraded by up to a factor of five. 3) The fraction of bulge-dominated systems in these groups is higher than in the field ($\sim 50\%$ vs. $\sim 20\%$). 4) The fraction of bulge-dominated systems in groups decreases with increasing radius, similar to the morphology-radius (\sim density) relation observed in galaxy clusters. 5) Current star formation in group galaxies is correlated with significant morphological asymmetry for disk-dominated systems ($B/T < 0.4$). 6) The group galaxies that are most disk-dominated ($B/T < 0.2$) are less star forming and asymmetric on average than their counterparts in the field.

Subject headings: galaxies: fundamental parameters – galaxies: structure – galaxies: clustering – galaxies: evolution

1. Introduction

How the evolution of galaxies is affected by environment continues to be a fundamental question in astronomy. Recent work by Schade *et al.* (1995, 1996), Abraham *et al.* (1996a, 1996b), Ratnatunga *et al.* (1999), and Simard *et al.* (1999, 2000) has focused on quantifying the morphologies of galaxies and relating them to environment and spectral star formation indicators. These efforts concentrate on field or cluster galaxies. Little has been done to quantitatively characterize galaxies in the intermediate, and common, environment of poor groups where the factors that might influence galaxy evolution differ from those in clusters or the rarefied field. One puzzle is that some poor groups with extended X-ray emission share certain properties with rich clusters, such as the shape of the galaxy luminosity function (Zabludoff & Mulchaey 2000) and a high early-type galaxy fraction (Zabludoff & Mulchaey 1998), but have lower velocity dispersions and galaxy number densities. By fitting 2D surface brightness profiles and examining the residual light after the model is subtracted, it now is possible to derive structural parameters for a large sample of group galaxies that may then be compared with results from other environments and with the galaxies' spectral properties. In particular, we can quantitatively and uniformly type galaxies by their bulge fraction, determine the fraction of galaxies with significant asymmetry, measure whether groups have a morphology-radius (\sim density) relation like clusters, compare group galaxy morphologies with the field, and assess whether the current star formation level in group galaxies is different than that in field galaxies of the same type.

As group galaxy number densities are closer to that of the field than of rich clusters, do the group galaxy populations differ significantly from the field? Early-type galaxies are the minority in the field, making up only $\sim 23\text{--}29\%$ of the field population (van den Bergh *et al.* 1996; Driver

et al. 1995; Shapley & Ames 1932). Given the morphology-density relation and the low galaxy number densities and velocity dispersions of groups, it is surprising that high early-type fractions consistent with those of rich clusters have been found in some X-ray detected groups (Mulchaey & Zabludoff 1998). Others (Hickson, Kindl, & Auman 1989; Williams & Rood 1987) also have found that approximately 50% of galaxies in compact groups are bulge-dominated systems. These studies show that the relationship between environment and galaxy type is still unclear. A limitation to understanding the link between galaxy morphology and environment in all these studies is how the galaxies are typed. Typing was usually done by eye and information like star-forming regions, tidal tails, and shells were noted but not included in a quantitative analysis. In addition, not only are there variations dependent on the author (*e.g.* Fabricant, Franx, & van Dokkum 2000) but visual typing is difficult to do consistently for a sample with hundreds of galaxies. An important first step in improving our understanding of what determines galaxy morphology in different environments is to type galaxies in a uniform and reproducible way so that we can compare these galaxies in a quantitative manner.

An important aspect of understanding how galaxy morphology depends on environment is observing how the early-type fraction in groups varies, if at all, with position *within* the group. Although the morphology-density relation has been well-established for clusters (Dressler 1980; Whitmore & Gilmore 1991) and has been studied for groups found in redshift surveys (Ramella *et al.* 1999; Postman & Geller 1984), the former is defined for regions of much higher density and larger physical volume than that of poor groups and the latter is defined by the *average* galaxy density of a group rather than as a function of position *within* the group. The morphology-radius (\sim density) relation has not been examined in poor groups, particularly those with extended X-ray emission that are likely to be real, bound systems. Our large sample of galaxies projected within the virial radii of the poor groups, coupled with the quantitatively derived morphologies, makes it possible to test if a morphology-radius (\sim density) relation also exists in these groups.

We extend our analysis by testing how environment affects galaxy formation and/or evolution by observing whether the star formation levels and degree of morphological disruption in these galaxies change with environment. We address these questions in a detailed manner by comparing only galaxies of the same morphological type. In past studies, it was not possible to make this clean a comparison since we lacked a uniform classification scheme and a sample large enough to be cut into statistically meaningful subsamples. With our large sample of spectroscopically-confirmed group members and quantitative measurement of physical galaxy characteristics, however, we now can use the bulge fraction to roughly isolate group galaxies of a particular, narrow class and to then compare their current star formation and asymmetry to their counterparts in the field.

In this paper, we characterize 171 galaxies in six nearby, X-ray detected, poor groups and 18 galaxies in the field using a new automated program that fits a PSF-convolved 2D surface brightness profile to an image of each galaxy and searches χ^2 space for the best model (GIM2D; Simard *et al.* 2000; Simard *et al.* 1999; Marleau & Simard 1998). For each group, we have 15 to 38 spectroscopically confirmed members ranging in luminosity from dwarfs to giants ($-13.7 \geq$

$M_R - 5\log h \geq -21.9$) and in Hubble type from irregulars and Sd's to S0's and ellipticals. By fitting two component profiles, we measure galaxy properties such as bulge fraction, half-light radius, and the fraction of light in an asymmetric component. These structural parameters allow us to type the galaxy as bulge or disk-dominated and to define its asymmetry in a quantitative and reproducible manner. Assuming a simple model, *e.g.* a de Vaucouleurs (de Vaucouleurs 1948) bulge and exponential disk, we determine the goodness of each fit and check the robustness of our results for galaxies imaged at different effective resolutions. We then compare the distributions of structural parameters and their relationship to current star formation (as measured by the 3727 Å [OII] emission line) for the group and field samples.

The sections of this paper are organized in the following manner: The data and the fitting technique are described in §2. Also included in §2 is an explanation of how we move all the galaxies to a common redshift ($cz_0 = 9000 \text{ km s}^{-1}$) and effective resolution ($0.87h^{-1} \text{ kpc}$) so that the samples may be directly compared. In §3, we present the models and structural parameters fit by GIM2D for the group and field galaxies at their original and common redshift. We also test for relationships among the bulge fraction, asymmetry, and the current star formation, discussing differences between the group and field populations. In §4, we discuss possible explanations for these differences. Our conclusions are summarized in §5. In this paper, we use $H_0 = 100h \text{ km s}^{-1} \text{ Mpc}^{-1}$ and $q_0 = 0.5$.

2. Observations and Analysis

2.1. Observations

We obtained images of the six galaxy groups (HCG 42, HCG 62, NGC 2563, NGC 3557, NGC 4325, and NGC 5129) with the Tektronix 2048² CCD and Swope 40'' telescope combination at Las Campanas Observatory during October 1996 and February 1997. Each image has a $\sim 23.8'$ field of view, and we constructed a 3×3 mosaic covering a $1^\circ \times 1^\circ$ field for each group. The pixel scale is $0.''696$. Each of the nine tiles in the mosaic overlap by $\sim 5'$ with an adjacent tile. With the Kron-Cousins R filter, each tile was exposed for a total time of 300 seconds. The seeing varied for each group, ranging from $1.''2$ to $2.''6$. We reduced the images using standard IRAF techniques.

We obtained complimentary spectra for group and field galaxies with the multi-fiber spectrograph (Shectman *et al.* 1992) and the 2D-Frutti detector mounted on the du Pont 2.5 m telescope at the Las Campanas Observatory. The spectra in this paper are a subset of those in Zabludoff & Mulchaey (1998a; 2000) and are described there. The spectra have a pixel scale of $\sim 3\text{Å}$, a resolution of $\sim 5 - 6\text{Å}$, and a wavelength range of $3500 - 6500\text{Å}$. The [OII] equivalent widths were measured in the same manner as in Zabludoff *et al.* 1996. At $m_R = 16$, the galaxy groups are 80–100% spectroscopically complete (Zabludoff & Mulchaey 2000). As the completeness function drops beyond $m_R \sim 17$, we consider only galaxies with $m_R < 18$; the absolute magnitude range for the sample is then $-13.7 \geq M_R - 5\log h \geq -21.9$. The absolute magnitude ranges are consistent

for the group and field samples (Fig. 3, top panel). Nevertheless, in comparing the groups with the field, we test our results for both the full absolute magnitude range and $M_R \leq -17 + 5\log h$ subsamples to account for any dependence on galaxy luminosity.

The group properties are listed in Table 1. For the field sample, there are 18 galaxies with $m_R < 18$ and $cz_0 < 9000 \text{ km s}^{-1}$; the field galaxies were serendipitous observations in the fore/background of the galaxy groups. The limit of $cz_0 < 9000 \text{ km s}^{-1}$ is the redshift to which we move our entire sample (group and field galaxies) for comparison (see §2.3).

2.2. Structural Measurements

We use the program GIM2D (Marleau & Simard 1998; Simard *et al.* 1999; Simard *et al.* 2000) to find the best-fit PSF-convolved, 2D bulge+disk models to the surface brightness profiles of 171 group and 18 field galaxies. The program has a maximum of 12 fitting parameters: the flux (F_{total}) in the model integrated to $r = \infty$; the bulge fraction $B/T \equiv F_{bulge}/F_{total}$; the semi-major axis effective radius of the bulge r_e ; the bulge ellipticity $e \equiv (1 - b)/a$ where a and b are the bulge semi-major and semi-minor axes respectively; the bulge position angle ϕ_b ; the semi-major axis exponential disk scale length r_d ; the inclination of the disk i ($i \equiv 0$ for face-on); the disk position angle ϕ_d ; the subpixel dx and dy offsets of the galaxy’s center; the residual background level db ; and the Sérsic index n of the bulge. Both ϕ_b and ϕ_d are measured clockwise from the positive y -axis of the image. Twelve parameters is a maximum as one or more parameters can be frozen to their initial values if necessary depending on the scientific goals being pursued. The best-fit parameters and their confidence intervals are determined using the Metropolis algorithm (Metropolis *et al.* 1953; Saha & Williams 1994) which uses the χ^2_ν test to determine the region of maximum likelihood in the multi-parameter space.

The bulge profile is defined as

$$\Sigma(r) = \Sigma_e \exp \left\{ -k[(r/r_e)^{1/n} - 1] \right\} \quad (1)$$

where $\Sigma(r)$ is the surface brightness at r along the semi-major axis, and Σ_e is the effective surface brightness. This bulge profile is also known as the Sérsic profile (Sérsic 1968). The parameter k is equal to $(1.9992n - 0.3271)$, a value that defines r_e to be the projected radius enclosing half of the light in the bulge component (Capaccioli 1989). The classical de Vaucouleurs profile is a special case of Equation 1 with $n = 4$.

The disk profile is defined as

$$\Sigma(r) = \Sigma_0 \exp(r/r_d) \quad (2)$$

where Σ_0 is the central surface brightness. We note as Simard *et al.* (1999, 2000) do that the bulge/disk nomenclature adopted here to describe our surface brightness models may not reflect the internal kinematics of its components. A “bulge” may not be a centralized, dynamically hot spheroid but a central starburst. Similarly, a “disk” may not necessarily be a cold, co-rotating

population. Some systems such as dwarf ellipticals are made up of a dynamically hot component with an exponential surface brightness profile.

Recent work (Courteau, de Jong, & Broeils 1996; Andredakis 1998) advocates a combination of two $n = 1$ exponential components to fit the surface brightness profile of late-type spirals. It is unclear from our analysis, however, that this profile is more appropriate than the classical de Vaucouleurs bulge plus exponential disk for the galaxies in our sample. We do fit a double exponential profile to galaxies in all six group mosaics and compare the results to those of the de Vaucouleurs bulge plus exponential disk models. Both profiles fit our galaxies equally well. Only 6/189 galaxies are marginally better fit by a double exponential profile; these range in magnitude from $15 < m_R < 17.4$ and in bulge fraction from $0 \leq (B/T)_{deV} \leq 0.9$. In the absence of a clear preference between the two bulge profiles and knowing that bright ellipticals and the bulges of early-type spirals are well-fit by a de Vaucouleurs profile (Andredakis 1998; Andredakis, Peletier, & Balcells 1995), we adopt this bulge profile plus an exponential disk as our canonical fitting model for the sake of continuity across the full range of morphological types.

Before GIM2D can fit a 2D model to the surface brightness of a given galaxy, the isophotal area of the galaxy and the point spread function (PSF) of the image at the location of the galaxy must first be determined. To define the isophotal area, we use the galaxy photometry package SExtractor V2.0 (Bertin & Arnouts 1996) with a detection threshold of $\mu = 24.05$ mags/ \square'' , a minimum deblending contrast parameter of 0.005, and two background mesh sizes corresponding to galaxies brighter and fainter than $m_R = 13$ (200 and 64, respectively). A variable mesh size is necessary since SExtractor can mistake the flux of extended objects for sky if the mesh size is too small and can thus over-subtract the sky from the object. We use the stand-alone version of DAOPHOT (Stetson 1987) to measure and generate a PSF for each galaxy. The PSF varies across the image, and these PSF variations are mapped as a function of position using stars located throughout the images. PSF models are then generated with DAOPHOT at regular intervals across the chip (every 50 pixels), and the PSF model closest to each galaxy is selected for its GIM2D analysis.

By fitting models to the surface brightness distribution of these galaxies, we measure the structural properties B/T , r_e , r_d , ϕ_b , ϕ_d , i , and the half-light radius $r_{1/2}$. The semi-major axis half-light radius is computed by integrating the sum of Equations 1 and 2 to $r = \infty$. The asymmetric image residual flux is quantified by GIM2D using the R_A index (Schade *et al.* 1995) defined as

$$\begin{aligned} R_A &= (R_A)_{raw} - (R_A)_{bkg} \\ &= \frac{\sum_{i,j} \frac{1}{2} |R_{ij} - R_{ij}^{180}|}{\sum_{i,j} I_{ij}} - \frac{\sum_{i,j} \frac{1}{2} |B_{ij} - B_{ij}^{180}|}{\sum_{i,j} I_{ij}} \end{aligned} \quad (3)$$

where R_{ij} is the flux at (i, j) in the residual image, R_{ij}^{180} is the flux in the residual image rotated by 180° , and I_{ij} is the flux in the original image. Following Marleau & Simard (1998), R_A is

measured within $r = 2r_{1/2}$. The second term $(R_A)_{bkg}$ in Equation 3 is a statistical correction for background noise fluctuations. Since $(R_A)_{raw}$ involves taking absolute values of pixel fluxes, it will yield a positive signal even in the sole presence of noise. The background correction, $(R_A)_{bkg}$, is computed over pixels flagged as background pixels in the SExtractor segmentation image. The B_{ij} ’s are background pixel values in the residual image, and the B_{ij}^{180} ’s are background pixel values in the residual image rotated by 180° . The background correction is computed over a background pixel area equal to the pixel area over which $(R_A)_{raw}$ is computed. Given the statistical nature of $(R_A)_{bkg}$, there will be cases when a galaxy is faint enough compared to its background noise that R_A may take on small negative values in exactly the way as the difference of two values of $(R_A)_{bkg}$ computed from different regions of the sky may be negative.

In addition to R_A , we measure the total residual fraction of light R_T by taking the pixels assigned to the galaxy by SExtractor and creating a mask that is applied to the original and model images. For a positive-definite residual fraction, the model is subtracted from the original and the absolute value of the differences are summed. To account for the sky, the same number of sky pixels as galaxy pixels are summed in the same manner and subtracted from the total galaxy residual. We use the total residual fraction of light as a gauge of the model’s goodness of fit but note that, for fainter galaxies, the error in R_T is dominated by the error in the flux.

2.3. Moving Galaxies to a Common Redshift

In our analysis, individual groups are compared with each other and with the field to test for differences among the group and field populations. To ensure that systematic biases in our quantitative classification affect all galaxies in our sample in the same way, we must observe all galaxies at the same effective resolution. As the galaxies lie at different distances and are imaged at different seeings, we artificially adjust each galaxy image to a common redshift and seeing by first reducing the galaxy’s flux, changing the seeing as the atmosphere then does, and finally binning the flux as a CCD detector does. This sequence thus mimics the real observations. The effective resolution is the physical radius of the seeing disk and is determined by a combination of the distance (redshift) and seeing. For example, the seeing in an image of the most distant group in our sample, NGC 4325 ($cz = 7558 \pm 70 \text{ km s}^{-1}$; Zabludoff & Mulchaey 1998a) is $1.''3$ and has an effective resolution of $0.46h^{-1} \text{ kpc}$. By moving the galaxies to a common, higher redshift, we also test the robustness of our results by comparing the galaxy models before and after the galaxies are moved back and the physical resolution of the image degraded.

We select a common redshift of $cz = 9000 \text{ km s}^{-1}$, a slightly higher redshift than our most distant group. We first fade the galaxies in each group by

$$F = \left[\frac{D_L(z_{9000})}{D_L(z_{fig1})} \right]^2 \quad (4)$$

where F is the fading factor, and $D_L(z_{9000})$ and $D_L(z_{fig1})$ are the cosmological luminosity distances

to $cz = 9000 \text{ km s}^{-1}$ and the group’s redshift respectively. Since the seeing for each image is different, we convolve each image with a gaussian whose σ is

$$\sigma = \frac{[(FWHM_T)^2 - (FWHM_I)^2]^{1/2}}{2.35} \quad (5)$$

where $FWHM_I$ is the image’s original full-width at half-maximum and $FWHM_T$ is the target full-width at half-maximum. $FWHM_T$ is set by NGC 5129, the group with the least effective resolution ($0.87h^{-1} \text{ kpc}$); $FWHM_T = 2.''1$ for $cz = 9000 \text{ km s}^{-1}$. The images then are binned (conserving flux) by

$$B = \left\lceil \frac{D_A(z_{9000})}{D_A(z_{fig1})} \right\rceil \quad (6)$$

where B is the size of the bin in pixels, and $D_A(z_{9000})$ and $D_A(z_{fig1})$ are the cosmological angular distances to $cz = 9000 \text{ km s}^{-1}$ and the group’s redshift respectively. By fading and binning the images, the sky noise is decreased; we add ~ 10 counts of Poisson noise to the reflxed and binned images so that the sky noise is the same as in the original images. The same process is applied to each field galaxy.

3. Results

3.1. The Models

We fit a de Vaucouleurs bulge with exponential disk model to the group and field galaxies at their original redshifts and at a common redshift of $cz = 9000 \text{ km s}^{-1}$. Table 2 lists the reference number, redshift, absolute magnitude (M_R), [OII] equivalent width (EW), bulge fraction (B/T ; average error ~ 0.1), half-light radius ($r_{1/2}h^{-1} \text{ kpc}$; average error $\sim 10\%$), asymmetry parameter (R_A ; average error ~ 0.02), and fraction of residual light (R_T ; average error ~ 0.02) for the field galaxies at their observed (cz_0) and common ($cz = 9000 \text{ km s}^{-1}$) redshifts; Table 3 lists the same parameters for the group galaxies. In Fig. 1a, we show all the galaxies (189) in the $1^\circ \times 1^\circ$ mosaic for the six galaxy groups. The pixel area in each galaxy thumbnail is 12 times the galaxy’s isophotal area as defined by SExtractor. In these images, the seeing ranges from $1.''3$ to $2.''6$. The galaxies range in magnitude from $-13.7 + 5$ to $-21.9 + 5\log h$. M_R is listed in the upper left corner of each thumbnail and the reference number in the lower left. Fig. 1b contains the best-fit de Vaucouleurs with exponential disk model for each galaxy; B/T is listed in the upper left corner of each thumbnail. The galaxies span the range in bulge fraction ($0 \leq B/T \leq 1$). Fig. 1c contains the residual images created by subtracting the best-fit models from the original images. Included in these thumbnails are the asymmetry parameter R_A and total residual fraction R_T .

In Fig. 2a, the same galaxies as in Fig. 1a are shown but after being moved to $cz = 9000 \text{ km s}^{-1}$ and the same effective resolution ($0.87h^{-1} \text{ kpc}$). As in Fig. 1, the thumbnails include M_R , B/T , R_A , R_T , and reference number. The effective resolution of $0.87h^{-1} \text{ kpc}$ at

$cz = 9000 \text{ km s}^{-1}$ is set by NGC 5129, the group with the least effective resolution given its combination of observed seeing ($2.''6$) and distance ($cz = 6998 \pm 51 \text{ km s}^{-1}$). As expected, fading the galaxies, changing the PSF slightly, and rebinning the image has diminished many of the features seen prominently at cz_0 . In most cases, especially with small galaxies, R_T has decreased due to the loss of spatial resolution. In a few extreme cases, B/T can change by as much as 0.59 (HCG 42-106), R_T as much as 0.30 (HCG 62-18), and R_A as much as 0.16 (HCG 62-18). We examine such changes more quantitatively in the next section.

3.1.1. How Good Are the Models?

From the 2D models fit by GIM2D to the surface brightness distributions of the galaxies in our sample, we see that most galaxies are fit well with the combination of a de Vaucouleurs bulge and exponential disk profile (cf. Figures 1b and 2b). Of the 189 galaxies in our sample, less than 10% of the galaxy’s light remains in the residual fraction for 158 galaxies (84%) at cz_0 and 171 galaxies (91%) at $cz = 9000 \text{ km s}^{-1}$. Galaxies with high residuals (Figures 1c and 2c) usually have bars, spiral arms, concentrated star-forming regions, warped disks, and tidal tails (see NGC 2563-18, NGC 5129-95, NGC 3557-5, NGC 2563-23, and NGC 2563-9 respectively), features that are impossible to fit with any smooth profile. We measure morphological asymmetries with R_A , a quantitative measure that facilitates comparison among the galaxies and their spectra.

A technical detail is how GIM2D tends to overestimate the disk component if there are bright features associated with it, *e.g.* spiral arms and HII regions (see NGC 2563-19, NGC 3557-5, and NGC 5129-6). This is a problem for all two-dimensional fitting programs using unsymmetrized images and affects mainly low B/T galaxies. Bright features in the disk cause GIM2D to overestimate the contribution from the disk component and increase its scale length r_d . Thus, the galaxy’s disk is oversubtracted and its B/T underestimated. These cases are easily identified by their high residual and asymmetry fractions.

Using the residual fraction of light (R_T) as a guide to the goodness of the models, we plot in Fig. 3 R_T as a function of absolute magnitude for both the original and redshifted galaxies. The dotted line denotes $R_T = 0$. The bottom panel shows the difference $[(R_T)_{cz_0} - (R_T)_{cz9000}]$ as a function of M_R for the group and field galaxies. The group and field galaxies are fit equally well with a de Vaucouleurs with exponential disk model across the range in absolute magnitude. As galaxies are redshifted and the seeing worsened, we would expect the fits to somewhat “improve” (*i.e.*, have smaller R_T) on average due to the loss of effective resolution. A comparison of the cz_0 and $cz = 9000 \text{ km s}^{-1}$ results shows that the fits to intrinsically faint (in general, small) galaxies do improve slightly when the galaxies are redshifted; the average $[(R_T)_{cz_0} - (R_T)_{cz9000}]$ is 0.02 ± 0.01 for galaxies fainter than $M_R = -20 + 5\log h$. For brighter (in general, bigger) galaxies, the ratio of the seeing disk to the galaxy size is relatively unaffected, and the number of pixels per galaxy remains large, from cz_0 to $cz = 9000 \text{ km s}^{-1}$.

3.2. Morphological Classifications

3.2.1. At the Observed Redshift (cz_0)

In Fig. 4, we compare the measured bulge fractions (B/T) for the field and group galaxies to their published Hubble types (from the NASA Extragalactic Database) to check for correspondence. The visually classified galaxies are split into four bins: Ellipticals (E); S0’s; Spirals/Barred Spirals (S/SB); and Irregular/Peculiar (Irr/Pec). Galaxies with significant asymmetry ($R_A \geq 0.05$) are circled. We note that only 24% of the entire sample has been visually typed and that the typing was done by different authors. It is clear from Fig. 4 that we cannot match the four morphological bins with four B/T bins. Instead, we use B/T to split the galaxies into “early” and “late” types, where the former are bulge-dominated galaxies and the latter are disk-dominated galaxies.

Comparing the Hubble type to the measured B/T for the non-redshifted and redshifted samples, we define the break between early and late-types at $B/T = 0.4$. As seen in Fig. 4, the bulge-dominated galaxies include a range of Hubble types, whereas the disk-dominated systems correspond to Hubble type spirals or irregulars. One discrepant galaxy is a field galaxy ($M_R = -16.4 + 5\log h$) classified in the literature as a dwarf elliptical but whose best-fit model is a pure disk ($B/T = 0$). Dwarf ellipticals have been found, however, to have exponential profiles (Ferguson & Bingelli 1994). Interestingly, the same galaxy was classified as a spiral by Zabludoff & Mulchaey (1998a; 1999). The 12 galaxies with S/SB Hubble types but with $B/T > 0.4$ were manually checked by two of the authors (K. T. and L. S.): ten have no visible disk and a de Vaucouleurs type profile, one has a prominent thick bar, and the last has a faint disk with a bright bulge. While the measured bulge fraction does not correspond to the published Hubble type for these 12 galaxies, the GIM2D models do match the galaxies’ images well.

3.2.2. At a Common Redshift ($cz = 9000 \text{ km s}^{-1}$)

The lower panel of Fig. 4 shows B/T and the Hubble types for the redshifted sample. The distribution is similar to that at cz_0 . We test the robustness of our results by examining the change in bulge and asymmetry fraction for galaxies in the two morphological bins. Fig. 5 shows how B/T and R_A change when group galaxies are redshifted to $cz = 9000 \text{ km s}^{-1}$. The galaxies are divided into bulge ($B/T \geq 0.4$) and disk-dominated ($B/T < 0.4$) galaxies. They are binned in cz with the median in each bin and the corresponding asymmetric 1σ confidence limits shown. There is no significant change in the median B/T for either bulge or disk-dominated group galaxies, even though some galaxies have been moved up to four times further away and the effective resolution degraded. B/T is stable for the bulk of the sample but a few outliers change significantly by either decreasing or increasing in B/T : 13/87 of $(B/T)_{cz_0} < 0.4$ galaxies have $(B/T)_{cz9000} \geq 0.4$ while 11/85 of $(B/T)_{cz_0} \geq 0.4$ have $(B/T)_{cz9000} < 0.4$. Classifying galaxies by their bulge fraction is thus robust on average for the sample but B/T (*i.e.*, classification) for individual galaxies may change

by up to 0.6.

3.3. The Fraction of Bulge-Dominated Galaxies ($B/T \geq 0.4$)

In Fig. 6 we show the bulge fraction distributions for the group and field galaxies at their original and common redshift. The B/T distribution in the groups is different than that in the field. Application of the Kolmogorov-Smirnov test (Press *et al.* 1992) rules out a common parent distribution with $> 95\%$ certainty at cz_0 and $cz = 9000 \text{ km s}^{-1}$. As we do not sample the same physical volume in all the groups, however, we test this result by including only galaxies within $R = 0.25h^{-1} \text{ Mpc}$ of their group centers. This projected distance limit is selected based on the radius corresponding to the $1^\circ \times 1^\circ$ field for the closest group, NGC 3557. Again, a common parent distribution for the field and groups is ruled out with $> 95\%$ certainty.

With the separation between early and late-type galaxies defined at $B/T = 0.4$, we find that the groups have a higher fraction of early-type galaxies than the field ($86/171=50\%$ vs. $3/18=17\%$ at $cz = 9000 \text{ km s}^{-1}$). This result is roughly consistent with those obtained by visual classification of compact group galaxies (cf. Rood & Williams 1989; Hickson, Kindl, & Huchra 1988; Zabludoff & Mulchaey 1998). A high early-type fraction is found in the individual groups as well as for the entire group sample. Moving the galaxies from cz_0 to a common redshift and effective resolution does not change the result significantly even though the effective resolution is decreased by as much as five for some galaxies. Including only galaxies within $0.25h^{-1} \text{ Mpc}$ of the groups' centers only increases the early-type fraction. These values are listed in Table 4.

We also test that the early-type fraction in groups and in the field are significantly different in the following manner. We calculate the probability that the group and field early-type fractions are the same by using the cumulative binomial probability distribution to determine whether there is a “parent” early-type fraction consistent with both the field and group early-type fractions. For example, suppose that k_1/n_1 is the observed fraction of group galaxies that are early-types and $k_2/n_2 < k_1/n_1$ is the observed fraction of field galaxies that are early-types. For each parent probability $p = 0$ to 1, we calculate the probability P_1 that *at least* k_1 of n_1 group galaxies are early-types,

$$P_1 \equiv \sum_{j=k_1}^{n_1} \binom{n_1}{j} p^j (1-p)^{n_1-j} = I_p(k_1, n_1 - k_1 + 1), \quad (7)$$

where I_p is the incomplete beta function (Press *et al.* 1992). For the same p , where p is the probability of event occurring per trial, we calculate the probability P_2 that *at most* k_2 of n_2 field galaxies are early-types,

$$P_2 \equiv 1 - I_p(k_2 + 1, n_2 - k_2). \quad (8)$$

The product of the probability distributions $P_1(p)P_2(p)$ is the joint probability distribution whose maximum tells us the likelihood that both k_1/n_1 and k_2/n_2 were drawn from the same parent

fraction. The probability that the early-type fraction of the group galaxies is the same as that of the field galaxies is 0.0019 (*i.e.*, significantly different at the $> 95\%$ level).

A possible caveat is the incompleteness of our sample at fainter magnitudes ($M_R > -17$). To test the result’s robustness, we impose a magnitude limit of $M_R \leq -17$ on the group and field galaxies. This decreases the group sample to 132 galaxies and the field to 14. With this limit, the galaxy groups are 80-100% complete. Again, we find that groups have a significantly higher fraction of early-type galaxies than the field: 67/132 (51%) to 3/14 (22%) at $cz = 9000 \text{ km s}^{-1}$.

3.4. The Spatial Distribution of Bulge-Dominated Galaxies

The B/T parameter permits us to test whether a morphology-radius (\sim galaxy density) relationship, similar to that of galaxy clusters (Dressler 1980; Whitmore & Gilmore 1991), exists in poor groups. In the five groups for which our sampling extends beyond projected radii of $R > 0.25h^{-1}$ Mpc (HCG 42, HCG 62, NGC 2563, NGC 4325, and NGC 5129), the early-type fraction decreases when all the group galaxies in the $1^\circ \times 1^\circ$ field are included. In Fig. 7, the bulge fraction measured at $cz = 9000 \text{ km s}^{-1}$ for all group members (171) is shown as a function of their projected radius from the fiber field center ($0 \geq R \geq 0.6h^{-1}$ Mpc). The least-squares fit to the data and the average B/T for each $50h^{-1}$ kpc bin both show a decrease in B/T with increasing projected distance from the group center. Using the Spearman rank test (Press *et al.* 1992), we find the anti-correlation between R and B/T to be $> 95\%$ significant.

The morphology-radius relation, high fraction of early-types, and diffuse X-ray halos of these groups also are observed in galaxy clusters. These points suggest that X-ray detected poor groups may form as low mass analogs of rich clusters (cf. Mulchaey & Zabludoff 1998).

3.5. The Fraction of Asymmetric Galaxies ($R_A \geq 0.05$)

As discussed in §2.2, GIM2D also quantifies galaxy asymmetry (R_A). Asymmetric features including tidal tails, shells, warped disks, and asymmetrically distributed HII regions increase R_A . After visually inspecting the galaxies and their residual images, we find that all of the galaxies with $R_A \geq 0.05$ have a visually obvious asymmetric residual light distribution (see 1c and 2c). Therefore, we adopt $R_A \geq 0.05$ as the lower limit for galaxies that we classify as having high galaxy asymmetry.

At $cz = 9000 \text{ km s}^{-1}$, the fraction of asymmetric galaxies is 19/171 (11%). We test for any radial or luminosity dependence in the asymmetry fraction by imposing the same radial and magnitude limits as in §3.3. Including only galaxies within $0.25h^{-1}$ Mpc of the group’s center does not change significantly the asymmetry fraction in the groups, nor does applying a magnitude limit of $M_R \leq -17$. It is not feasible to compare the asymmetry fraction of individual groups because

we are limited by the small number of asymmetric members in each group.

Comparing the results for the original and redshifted galaxies, we observe a slight decrease in the ability to recover asymmetric features with decreased effective resolution (Fig. 5): the mean change is 0.02 ± 0.01 at all cz_0 for the entire group sample. We note that 13/24 (54%) of the galaxies with $(R_A)_{cz_0} \geq 0.05$ are not considered significantly asymmetric after they are moved to $cz = 9000 \text{ km s}^{-1}$. This result is due to the decrease in effective resolution and the loss of morphological information. Of the 147 cz_0 galaxies with $R_A < 0.05$, however, eight (5%) are considered significantly asymmetric at $cz = 9000 \text{ km s}^{-1}$. In this case, the fading of the galaxy images makes asymmetries more prominent by reducing the contribution from the lower surface brightness, symmetric component. As in the case of B/T , there are as many outliers whose R_A increases as there are whose R_A decreases such that the average change in R_A is fairly small, even though R_A for individual galaxies can change by as much as 0.16. The asymmetry index measured does correspond to the galaxy’s image but the question of whether the image truly reveals the galaxy’s properties becomes increasingly important with increasing redshift.

In Fig. 8, the distribution of R_A with respect to B/T for the groups and the field at $cz = 9000 \text{ km s}^{-1}$ is shown. The lower panel shows the fraction of group galaxies with high galaxy asymmetry ($R_A \geq 0.05$) for each B/T bin. There is no correlation between R_A with B/T in these groups (the results are similar at cz_0). Group members with high galaxy asymmetry are not even predominantly disk-dominated systems: 10/19 of the significantly asymmetric group galaxies at $cz = 9000 \text{ km s}^{-1}$ have $B/T \geq 0.4$.

Of the asymmetric disk-dominated systems, 8/9 (89%) are star forming (see §3.6). Thus, their high R_A values most likely result from (1) asymmetrically distributed HII regions, (2) interaction-induced features, and/or (3) the presence of a close companion inside the $2r_{1/2}$ aperture used to calculate R_A (no close companions are visible, however). In contrast, none of the asymmetric bulge-dominated galaxies at $cz = 9000 \text{ km s}^{-1}$ are star-forming. Thus, their high R_A value may result only from the latter two explanations. Unlike the disk-dominated systems, 3/10 asymmetric bulge-dominated galaxies do have close companions (HCG 62-1, HCG 62-4, and HCG 62-18).

To test for differences between the asymmetry fraction of the groups and the field, we consider only a narrow class of disk-dominated galaxies ($B/T < 0.2$). Because group galaxies have a higher B/T on average than field galaxies (§3.3), selecting a narrow range of B/T allows us to first remove any dependence of R_A on B/T (however small). The range $B/T < 0.2$ is chosen because it contains most of the field sample and thus the statistics for a field/group comparison are best within this B/T range. Using the cumulative binomial probability distribution (§3.3), we find that for these strongly disk-dominated galaxies the field asymmetry fraction ($6/13 = 46\%$) differs from that of groups ($7/52 = 13\%$) at the $> 95\%$ confidence level (see Fig. 9). Thus, not only do group galaxies tend to have higher bulge fractions than field galaxies but the most disk-dominated group galaxies are less asymmetric on average than their counterparts in the field.

3.6. Current Star Formation

3.6.1. B/T vs. $[OII]$ Emission

In the following discussion, we compare the $[OII]$ emission with the structural parameters measured using GIM2D for the composite group and the field galaxies. From the spectra, we have the $[OII]$ flux estimate and equivalent width (EW); we use the former to define a star-forming galaxy and the latter as a measure of the star formation rate (Kennicutt 1992; Balogh *et al.* 1999). Note that we assume $[OII]$ emission indicates star formation and not AGN activity. For uniformity, we consider only results for the redshifted ($cz = 9000 \text{ km s}^{-1}$) sample because we focus on the comparison of the composite group with the field. Figure 10 shows B/T , $[OII]$ EW, and the asymmetry R_A versus absolute magnitude (M_R). From this figure, it is clear that B/T , $[OII]$ EW, and R_A vary with galaxy luminosity. Therefore, it is possible to obtain misleading results by comparing samples with different luminosity ranges or by considering only the brightest galaxies. We stress that our group and field samples have similar absolute magnitude ranges, and that including only galaxies brighter than $M_R = -17 + 5\log h$ does not affect our overall results.

In Fig. 11 the $[OII]$ EW is plotted against B/T for the group and field galaxies. The upper panel shows the $[OII]$ EW distribution versus B/T . The lower panel shows the fraction of group galaxies with $[OII]$ *flux* greater than 2σ where σ is the error in the flux. Current star formation often is associated with late-type galaxies (Hashimoto *et al.* 1998; Kennicutt 1992), and comparison of the $[OII]$ emission to B/T in our redshifted sample agrees with this finding. Of the 30 star-forming galaxies ($[OII]$ *flux* $\geq 2\sigma$), 22 are disk-dominated ($B/T < 0.4$) systems ranging in magnitude from -16.3 to $-20.3 + 5\log h$. Particularly interesting, however, is the fraction of star-forming galaxies that are bulge-dominated: 8 of 30 (27%) star-forming galaxies ranging in magnitude from -15.5 to $-20.9 + 5\log h$ have $B/T \geq 0.4$. The fraction of all bulge-dominated galaxies that are forming stars is small (8/86; 9%) but covers a large range in luminosity.

These 30 star-forming galaxies are not concentrated in the group centers but are $90\text{--}660h^{-1} \text{ kpc}$ away in projected radius. In comparison, quiescent group galaxies are $10\text{--}630h^{-1} \text{ kpc}$ from their group center. Application of the Kolmogorov-Smirnov test on the two radial distributions excludes a common distribution with $> 95\%$ confidence. Like Zabludoff & Mulchaey (1998), we find that galaxies with significant $[OII]$ emission tend to lie further from the projected group center than those with no significant emission. We note, however, that this result may be strongly correlated with the morphology-radius (\sim density) relation observed in these groups. For example, a K-S test of the radial distributions for the most disk-dominated ($B/T < 0.2$) star-forming and quiescent group galaxies (16 and 36 respectively) finds them to be indistinguishable.

3.6.2. Asymmetry vs. [OII] Emission

Disturbed galaxies often show signatures of current star formation in their spectra (Young *et al.* 1996), suggesting that the mechanisms that trigger bursts also can alter galaxy morphology. These starbursts are characterized by strong [OII] emission (Kennicutt 1992), which serves as a spectral snapshot of the galaxy’s current star-forming activity. If asymmetries are related to star formation, galaxies with strong [OII] emission should have higher R_A values. We test the link between recent star formation activity and the morphological characteristics of our sample galaxies by comparing their [OII] EW to the asymmetry parameter R_A . In Fig. 12 we show [OII] EW versus R_A for bulge-dominated ($B/T \geq 0.4$) and disk-dominated ($B/T < 0.4$) galaxies in the groups and the field at $cz = 9000 \text{ km s}^{-1}$.

There is a trend of increasing [OII] emission with increasing R_A for *disk-dominated* galaxies; the trend is $> 95\%$ significant using the Spearman rank test (Press *et al.* 1992). Two possible explanations of this correlation are: 1) an external cause such as a physical connection between asymmetry and star formation so that if a galaxy is morphologically disturbed by an external force like a merger or tidal interaction, its star formation also is elevated or 2) an internal cause such as asymmetrically distributed HII regions that will increase R_A (our code cannot distinguish between this case and a tidally disrupted galaxy).

We do not find a significant correlation between [OII] emission and high R_A for *bulge-dominated* group galaxies. We note, however, that this does not mean there is no link between high R_A and star formation for these galaxies. A correlation may exist but our ability to test for one is limited by the small fraction of these galaxies with significant [OII] emission. We also note that in Fig. 12, $B/T \geq 0.4$ objects with large [OII] EW’s and low R_A actually may be galaxies with central star-forming regions rather than a true bulge.

To test for differences between the star forming fraction of the groups and field, we again consider only objects in a narrow class of late-types ($B/T < 0.2$; see Fig. 9). In doing so, we maximize the statistics for a field/group comparison and remove any dependence between [OII] emission and B/T . In this B/T bin, the field and group star-forming galaxies have indistinguishable absolute magnitude ranges with the K-S test. Using the cumulative binomial probability distribution (§3.3), we find that for these strongly disk-dominated galaxies, the fraction forming stars is significantly higher ($> 95\%$ confidence) in the field than in the groups: 9/13 (69%) compared to 16/52 (31%). In addition, the field’s average [OII] EW for these galaxies is twice that of the groups: $14.3 \pm 0.5 \text{ \AA}$ compared to $7.4 \pm 0.4 \text{ \AA}$. Not only do group galaxies differ from the field in early-type fraction but for the most disk-dominated galaxies, the galaxy asymmetry, star formation fraction, and star formation rate are lower in groups (Fig. 9).

4. Discussion

The group galaxy populations in our sample differ from the field morphologically and in current star formation: 1) The early-type fraction in groups is higher than the field. 2) For the most disk-dominated systems, the fraction of galaxies that are asymmetric, the fraction that are star-forming, and the average [OII] EW in the galaxies are lower in groups than in the field. The first point is consistent with the predictions of standard biased galaxy formation (White 1994), in which more massive (typically, bulge-dominated) galaxies form in denser regions, and does not obviously require subsequent environment-dependent galaxy evolution. Possible explanations for the second point include:

I. Forming in regions of higher mass density than the field, groups collapse earlier and their galaxies may form earlier as well. Thus, a group late-type may have consumed more of its gas by the current epoch than a similar galaxy in the field, leading to less star formation and more symmetry in the group galaxy.

II. The environment of X-ray luminous groups might shut down star formation (and make galaxies look more symmetric), although processes such as ram pressure stripping are not thought to be as effective in group environments as in clusters due to the lower average velocity dispersions of groups (cf. Zabludoff & Mulchaey 1998). For some rich clusters, such environment-dependent evolution mechanisms are invoked to explain the lower average star formation activity in cluster galaxies relative to the field (Poggianti *et al.* 1998; Balogh *et al.* 1999).

III. Interactions and mergers between galaxies, which are known to enhance star formation (Young *et al.* 1996) and disrupt galaxy morphology (Mihos 1995), may occur more frequently outside of X-ray luminous groups and clusters at the current epoch. Although these groups are probable sites for interactions between galaxies because their velocity dispersions are comparable to those of individual group members (Barnes 1985; Aarseth & Fall 1980), mergers that could boost star formation and asymmetry are less likely today for two reasons. First, the predominance of early-types in X-ray luminous groups reduces the chance of any two gas-rich galaxies merging at the current epoch. Second, most of the group mass lies in a common halo rather than with individual galaxies (Zabludoff & Mulchaey 1998). This mass distribution reduces the cross-section of the galaxies and thus the merger rate (Athanasoula, Makino, & Bosma 1997). In such a model, if interactions occur they do so early in the group’s evolutionary history, and may be the reason for the predominance of quiescent, undisturbed early-type galaxies in X-ray luminous groups today.

5. Conclusions

Using multi-object spectroscopy and wide-field CCD imaging of six nearby X-ray detected, poor galaxy groups, we characterize the morphology and current star formation of the group members and of a comparison sample of field galaxies. The large number of spectroscopically confirmed

members in each group allows us to sample a wide range of galaxy types and luminosities, whereas most previous group studies have been limited to only the few brightest members. By objectively classifying the galaxies into early and late-types using their bulge fractions, quantitatively measuring the asymmetry of each galaxy, and determining the [OII] emission line strength, we also investigate the relationship between galaxy morphology and current star formation for galaxies in these common, yet poorly understood, environments.

We measure the structural parameters and morphologically classify 171 group members and 18 field galaxies. Surface brightness models are fit to the galaxies at their observed (cz_0) and at a common ($cz = 9000 \text{ km s}^{-1}$) redshift. By fitting 2D models to the galaxies at these two redshifts, the composite of the group sample can be compared directly to the field, and the robustness of the models is tested.

Our conclusions are as follows:

I. A de Vaucouleurs bulge with exponential disk model fits well the surface brightness profile of the group and field galaxies in our sample. Of the 189 galaxies in our sample, 172 (91%) have residual fractions < 0.1 once the model is subtracted (at $cz = 9000 \text{ km s}^{-1}$). Our ability to fit models to the data does not depend strongly on morphological type or luminosity. The majority of galaxies with high residuals have bars, spiral arms, tidal tails, star-forming regions, and dust lanes, features that cannot be fit with any smooth profile.

II. Morphologically classifying galaxies by bulge fraction (B/T) is fairly robust on average for the galaxies in our sample of nearby groups, even when the galaxy’s redshift is increased by up to a factor of four and the effective resolution degraded by up to a factor of five. The average asymmetry (R_A) of these galaxies decreases slightly at the higher redshift (0.02 ± 0.01). We note, however, that both B/T and R_A can change in either direction by as much as 59% and 30%, respectively, for individual galaxies.

III. The fraction of early-type ($B/T \geq 0.4$) galaxies in X-ray detected, poor groups is higher than the field ($\sim 50\%$ vs. $\sim 20\%$ at $cz = 9000 \text{ km s}^{-1}$). A common parent galaxy distribution for the group and field samples can be ruled out with $> 95\%$ certainty.

IV. Groups have a morphology-radius (\sim density) relation. The average B/T for the combined group sample decreases from the core out to $0.6h^{-1} \text{ Mpc}$. The anti-correlation between B/T and radius is $> 95\%$ significant using the Spearman rank test.

V. Current star formation, as characterized by [OII] emission, is correlated with high asymmetry ($R_A \geq 0.05$) for disk-dominated ($B/T < 0.4$) systems in the groups. Two possible explanations for this correlation are: (1) A physical connection between morphology and star formation exists such that when group galaxies are disturbed by an external force, their star formation also is boosted. (2) The fact that asymmetrically distributed HII regions will cause a high R_A (and that our code cannot distinguish between this case and, for example, a tidally disrupted galaxy). While we cannot always identify the sources of high asymmetry in disk, star-forming galaxies, there is less

ambiguity for quiescent early-types. There is a non-negligible fraction of early-type group galaxies ($10/86=12\%$) that are both asymmetric and quiescent – these are likely to be morphologically disturbed and/or to have a close companion.

VI. For the most disk-dominated galaxies ($B/T < 0.2$), the fraction with a high degree of asymmetry ($R_A \geq 0.05$) is significantly higher in the field than in groups ($6/13=46\%$ vs. $7/52=13\%$, respectively), the fraction that are forming stars is significantly higher in the field ($9/13=69\%$ vs. $16/52=31\%$, respectively), and the average star formation rate is significantly higher in the field ($14.3 \pm 0.5 \text{Å}$ vs. $7.4 \pm 0.4 \text{Å}$, respectively). These points suggest that although there are some highly disturbed-looking group galaxies in our sample, very late-type galaxies in X-ray detected groups are less star forming and asymmetric on average than similar galaxies in the field.

We are grateful to Katherine Wu for helpful discussions about quantifying galaxy morphologies and Chuck Keeton for useful discussions on statistics. We thank the anonymous referee for his helpful comments and quick response. K. H. T. thanks Garth Illingworth for his patience and Helmut Katzgraber for his unflagging support. This work was partially supported by NASA grant HF-01087.01-96A. This paper is based on observations made at Las Campanas Observatory, Chile.

REFERENCES

- Aarseth, S. J. & Fall, S. M. 1980, *ApJ*, 236, 43
- Abraham, R. G., Tanvir, N. R., Santiago, B. X., Ellis, R. S., Glazebrook, K., & van den Bergh, S. 1996, *MNRAS*, 279, L47
- Abraham, R. G., Smecker-Hane, T. A., Hutchings, J. B., Carlberg, R. G., Yee, H. K. C., Ellingson, E., Morris, S., Oke, J. B., & Rigler, M., 1996 *ApJ*, 471, 694
- Andredakis, Y. C., Peletier, R. F., & Balcells, M. 1995, *MNRAS*, 275, 874A
- Andredakis, Y. C. 1998, *MNRAS*, 295, 725
- Athanassoula, E., Makino, J., & Bosma, A. 1997, *MNRAS*, 286, 825
- Balogh, M. L., Schade, D., Morris, S. L., Yee, H. K. C., Carlberg, R. G., & Ellingson, E. 1999, *ApJ*, 504L, 75
- Barnes, J. 1985, *Nature*, 338, 123
- Bertin, E. & Arnouts, S. 1996, *A&A*, 117, 393
- Binney, J. & Tremaine, S. 1987, *Galactic Dynamics* (Princeton: Princeton University Press)
- Capaccioli, M. 1989, in *The World of Galaxies* (ed. Corwin, H. G. & Bottinelli, L.) 208 (Springer-Verlag, Berlin)
- Courteau, S., de Jong, R. S., & Broeils, A. H. 1996, *ApJ*, 457L, 73
- Davis, D. S., Keel, W. C., Mulchaey, J. S., & Henning, P. A. 1997, *AJ*, 114, 613

- de Vaucouleurs, G. 1948, *Ann. d'Astrophys.*, 11, 247
- Dressler, A. 1980, *ApJ*, 236, 351
- Driver, S. P, Windhorst, R. A., & Griffiths, R. E. 1995, *ApJ*, 453, 48
- Fabricant, Franx, & van Dokkum 2000, *ApJ*, *in press*
- Ferguson, H. C. & Bingelli, B., 1994, *A&A Rev.*, 6, 67
- Hashimoto, Y., Oemler, A., Lin, H., & Tucker, D. L. 1998, *ApJ*, 499, 589
- Hickson, P., Kindl, E., & Huchra, J. P. 1988, *ApJ*, 331, 64
- Hickson, P. Kindl, E., & Auman, J. R. 1989, *ApJS*, 70, 687
- Im, M., Simard, L., Koo, D. C., Faber, S. M., Gebhardt, K., Willmer, C. N. A., Phillips, A., Illingworth, G., Vogt, N. P., & Sarajedini, V. L. 2000, *in preparation*
- Kennicutt, R. C., 1992, *ApJ*, 388, 310
- Marleau, F. R. & Simard, L. 1998, *ApJ*, 507, 585
- Mendes de Oliveira, C., Plana, H., Amram, P., Bolte, M., & Boulesteix, J. 1998, *ApJ*, 507, 691
- Metropolis, N., Rosenbluth, A., Rosenbluth, M., Teller, A., & Teller, E. 1953, *Journal of Chemical Physics*, 21, 1087
- Mihos, C. 1995, *ApJ*, 438L, 75
- Moore, B., Katz, N., Lake, G., Dressler, A., & Oemler, A. 1996, *Nature*, 379, 613
- Pildis, R. A., Bregman, J. N., & Schombert, J. M. 1995, *AJ*, 110, 1498
- Pildis, R. A., Evrard, A. E., & Bregman, J. N. 1996, *AJ*, 112, 378
- Poggianti, B. M., Smail, I., Dressler, A., Couch, W. J., Barger, A. J., Butcher, H., Ellis, R. S., & Oemler, A. 1999, *ApJ*, 518, 576
- Postman, M. & Geller, M. J. 1984, *ApJ*, 281, 95
- Press, W. H., Teukolsky, S. A., Vetterling, W. T., & Flannery, B. P. 1992, *Numerical Recipes* (Cambridge: Cambridge University Press)
- Ramella *et al.* 1999, *A&A*, 342, 1
- Ratnatunga, K. U., Griffins, R. E., & Ostrander, E. J. 1999, *AJ*, 118, 86
- Rood, H. J. & Williams, B. A. 1989, *ApJ*, 339, 772
- Saha, P. & Williams, T. B. 1994, *AJ*, 107, 1295
- Schade, D., Lilly, S. J., Crampton, D., Hammer, F., Le Fèvre, O., & Tresse, L. 1995, *ApJ*, 451, L1
- Schade, D., Lilly, S. J., Le Fèvre, O., Hammer, F., & Crampton, D. 1996, *ApJ*, 464, 79
- Sérsic, J. L. 1968, *Atlas de galaxies australes*. Observatoria Astronomico, Cordoba
- Shapley, H. & Ames, A. 1932, *Harvard Ann.*, Vol. 88, No.2

- Shectman, S. A., Schechter, P. L., Oemler, A. A., Tucker, D., Kirshner, R. P., & Lin, H. 1992, in Clusters and Superclusters of Galaxies (ed. Fabian, A. C.) 351-363 (Kluwer, Dordrecht)
- Simard *et al.* 2000, *in preparation*
- Simard, L., Koo, D. C., Faber, S. M., Sarajedini, V. L., Vogt, N. P., Phillips, A. C., Gebhardt, K., Illingworth, G. D., & Wu, K. L. 1999, *ApJ*, 519, 563
- Stetson, P. B. 1987, *PASP*, 99, 191
- van den Bergh, S., Abraham, R. G., Ellis, R. S., Tanvir, N. R., Santiago, B. X., & Glazebrook, K. G. 1996, *AJ*, 112, 359
- White, S. D. M 1994, *Reviews in Modern Astronomy*, V7, 255-263
- Whitmore, B. C. & Gimore, D. M. 1991, *ApJ*, 367, 64
- Young, J. S., Allen, L., Kenney, J. D., Lesser, A., & Rownd, B. 1996, *AJ*, 112, 1903
- Zabludoff, A. I. & Mulchaey, J. S. 2000, *ApJ*, 539, 136
- Zabludoff, A. I. & Mulchaey, J. S. 1998a, *ApJ*, 496, 39
- Zabludoff, A. I. & Mulchaey, J. S. 1998b, *ApJ*, 498L, 5
- Zabludoff, A. I., Zaritsky, D., Huan, L., Tucker, D., Hashimoto, Y., Shectman, S. A., Oemler, A., & Kirshner, R. P. 1996, *ApJ*, 466, 104

Table 1. Group Properties ^a

Group	α (2000.0)	δ (2000.0)	N ^b	\bar{v}	σ	$D^c(h^{-1} \text{ kpc})$
NGC2563	8 20 24.4	+21 05 46	36	4775 \pm 65	336 \pm 44	811
NGC3557	11 09 58.5	-37 23 03	15	2843 \pm 64	282 \pm 50	488
NGC4325	12 23 18.2	+10 37 19	23	7558 \pm 70	265 \pm 50	1272
NGC5129	13 24 28.1	+13 55 32	34	6998 \pm 51	304 \pm 43	1173
HCG 42	10 00 13.1	-19 38 24	25	3830 \pm 47	266 \pm 37	654
HCG 62	12 53 12.4	-09 12 12	38	4356 \pm 50	376 \pm 52	741

^aThe values for α , δ , \bar{v} , and σ are from Zabludoff & Mulchaey 1999.

^bTotal number of group members in the $1^\circ \times 1^\circ$ field (Zabludoff & Mulchaey 1999).

^cPhysical diameter subtended by 1° at the group’s mean recessional velocity ($H_0 = 100h \text{ km s}^{-1}\text{Mpc}^{-1}$; $q_0 = 0.5$).

Table 2. Structural Parameters of Field Galaxies Measured at cz_0 and $cz = 9000 \text{ km s}^{-1}$

Field	ID	$cz_0 \text{ (km s}^{-1}\text{)}$	$M_R - 5\log h^a$	[OII] EW (Å)	cz_0				$cz = 9000 \text{ km s}^{-1}$			
					B/T ^b	$r_{1/2}^c \text{ (h}^{-1} \text{ kpc)}$	R_A^d	R_T^e	B/T	$r_{1/2} \text{ (h}^{-1} \text{ kpc)}$	R_A	R_T
H42	20	7611±37	-19.8	6.9±0.7	0.44	2.94	0.08	0.19	0.01	1.08	0.02	0.07
H42	25	8425±35	-19.3	3.7±0.9	0.18	4.93	0.04	0.06	0.03	2.11	0.08	0.08
H42	30	7555±12	-18.4	34.8±2.0	0.39	2.98	0.06	0.12	0.19	1.38	0.02	0.02
H42	131	7610±33	-17.1	22.1±1.6	0.19	1.21	0.02	0.04	0.19	0.62	0.08	0.10
H62	24	2266±40	-18.4	13.7±1.5	0.15	5.34	0.08	0.19	0.13	9.74	0.05	0.15
H62	42	7341±35	-18.6	34.8±2.2	0.15	2.73	0.07	0.08	0.16	1.62	0.05	0.05
N2563	15	6708±28	-20.3	0.5±1.0	0.93	2.29	0.03	0.10	0.56	1.51	0.02	0.04
N2563	17	6387±60	-19.6	2.3±1.2	0.04	3.14	0.08	0.14	0.02	2.26	0.04	0.12
N2563	22	6482±24	-19.8	4.9±1.2	0.41	2.78	0.04	0.07	0.48	2.22	0.02	0.03
N2563	48	6488±62	-18.3	20.6±4.5	0.03	2.04	0.04	0.07	0.00	1.51	0.01	0.03
N2563	86	6932±40	-17.8	12.2±1.7	0.09	2.53	0.06	0.08	0.00	1.69	0.00	0.01
N2563	88	2058±12	-15.3	41.9±14.8	0.25	0.60	0.03	0.08	0.53	1.87	0.01	0.04
N2563	152	2073±92	-14.4	-0.3±6.3	0.46	0.41	0.01	0.07	0.29	0.83	0.01	0.01
N4325	23	2067±104	-16.4	-0.1±2.0	0.00	1.84	0.02	0.04	0.00	6.48	0.00	0.02
N4325	47	904±59	-13.7	3.0±2.1	0.22	0.26	0.01	0.02	0.25	2.14	0.00	0.02
N4325	150	8151±40	-17.6	13.2±0.9	0.12	1.39	0.07	0.09	0.05	1.30	0.05	0.05
N4325	153	8256±34	-17.4	8.9±1.1	0.00	2.07	0.08	0.08	0.00	1.92	0.06	0.07
N4325	174	8146±40	-16.9	13.0±1.7	0.00	1.59	0.01	0.03	0.01	1.45	0.03	-0.00

^a $H_0 = 100 \text{ km s}^{-1}\text{Mpc}^{-1}$, $q_0 = 0.5$, flat cosmology

^bAverage error for B/T measurement is ~ 0.1 (Simard *et al.* 2000), although B/T can change by as much as 0.59 when the original (cz_0) and degraded ($cz = 9000 \text{ km s}^{-1}$) values are compared for individual galaxies.

^cAverage error for $r_{1/2}$ is $\sim 10\%$ (Simard *et al.* 2000).

^dAverage random error for R_A is ~ 0.02 (Simard *et al.* 2000; Im *et al.* 2000), although R_A can change by as much as 0.16 when the original (cz_0) and degraded ($cz = 9000 \text{ km s}^{-1}$) values are compared.

^eAverage random error for R_T is ~ 0.02 (Simard *et al.* 2000; Im *et al.* 2000), although R_T can change by as much as 0.30 when the original (cz_0) and degraded ($cz = 9000 \text{ km s}^{-1}$) values are compared.

Table 3. Structural Parameters of Group Galaxies Measured at cz_0 and $cz = 9000 \text{ km s}^{-1}$

Field	ID	$cz_0 \text{ (km s}^{-1}\text{)}$	$M_R - 5\log h^a$	[OII] EW (\AA)	cz_0				$cz = 9000 \text{ km s}^{-1}$			
					B/T ^b	$r_{1/2}^c \text{ (} h^{-1} \text{ kpc)}$	R_A^d	R_T^e	B/T	$r_{1/2} \text{ (} h^{-1} \text{ kpc)}$	R_A	R_T
H42	1	3950 \pm 30	-21.5	-0.4 \pm 0.7	0.73	6.49	0.02	0.03	0.84	6.43	0.03	0.08
	4	4176 \pm 25	-20.0	-0.5 \pm 0.7	1.00	2.75	0.02	0.13	0.56	2.16	0.01	0.04
	5	3980 \pm 23	-20.1	-0.0 \pm 0.6	1.00	1.44	0.05	0.17	0.74	1.69	0.02	0.06
	6	3538 \pm 46	-18.6	2.8 \pm 1.5	0.05	3.70	0.06	0.12	0.06	3.99	0.03	0.09
	7	4193 \pm 25	-19.8	-0.5 \pm 0.8	0.71	0.91	0.02	0.07	0.71	0.77	0.01	0.02
	9	3424 \pm 37	-18.6	5.7 \pm 1.5	0.57	1.04	0.02	0.02	0.52	1.11	0.02	0.04
	13	3504 \pm 36	-18.5	10.2 \pm 1.1	0.03	3.37	0.02	0.16	0.03	3.43	0.01	0.15
	14	3636 \pm 19	-18.9	-0.5 \pm 0.6	0.59	1.35	0.02	0.09	0.43	0.88	0.10	0.23
	15	4287 \pm 31	-18.2	22.1 \pm 1.5	0.30	3.42	0.08	0.13	0.22	3.25	0.05	0.10
	21	3675 \pm 29	-18.4	1.4 \pm 1.0	0.66	1.16	0.03	0.05	0.46	0.99	0.04	0.07
	22	3828 \pm 26	-17.9	0.8 \pm 1.0	0.31	1.48	0.01	0.03	0.22	1.54	-0.01	-0.00
	23	3613 \pm 27	-17.9	6.7 \pm 1.1	0.44	1.56	0.01	0.04	0.52	1.55	-0.00	0.00
	24	4076 \pm 80	-18.3	0.0 \pm 0.0	0.46	1.05	0.01	0.02	0.26	0.85	0.00	0.00
	28	3621 \pm 23	-17.8	-0.3 \pm 0.7	0.53	1.04	0.01	0.03	0.46	1.23	0.00	0.03
	29	3766 \pm 24	-17.6	0.2 \pm 0.6	0.46	0.98	0.01	0.03	0.41	0.99	-0.00	-0.00
	34	3876 \pm 39	-17.4	4.9 \pm 1.8	0.40	0.99	0.01	0.05	0.45	1.05	0.00	-0.00
	46	3891 \pm 39	-16.9	-1.0 \pm 0.5	0.79	1.37	0.02	0.03	0.38	1.47	0.02	0.02
	59	3647 \pm 59	-16.1	1.7 \pm 1.5	0.13	0.71	0.04	0.05	0.29	0.97	0.02	0.03
	65	3938 \pm 72	-16.4	5.0 \pm 2.5	0.52	0.97	0.02	0.04	0.22	0.97	0.01	0.01
	69	3675 \pm 27	-16.8	-0.4 \pm 0.6	0.50	0.37	0.01	0.03	0.55	0.41	-0.00	0.00
	85	3402 \pm 32	-15.7	7.4 \pm 1.2	0.00	0.74	0.00	0.04	0.51	1.24	-0.01	-0.01
	94	3732 \pm 75	-15.6	6.8 \pm 2.1	0.00	1.02	0.00	0.03	0.39	2.00	-0.03	0.08
	106	3924 \pm 132	-15.7	0.1 \pm 0.9	0.09	0.82	0.03	0.01	0.68	1.22	-0.07	-0.03
	136	4587 \pm 36	-15.7	57.9 \pm 16.1	0.15	0.99	0.00	0.05	0.43	1.03	-0.02	-0.02
	143	4081 \pm 43	-15.5	0.3 \pm 1.1	0.14	0.67	0.00	0.04	0.33	0.68	0.02	-0.01
H62	1	4284 \pm 31	-20.6	0.4 \pm 1.1	0.81	6.70	0.19	0.18	0.59	4.01	0.25	0.25
	3	3690 \pm 27	-19.9	3.1 \pm 1.2	0.74	3.68	0.04	0.14	0.83	4.64	0.05	0.17
	4	3555 \pm 28	-19.7	-0.3 \pm 0.7	0.80	1.17	0.04	0.25	0.45	3.40	0.05	0.07
	8	3565 \pm 14	-20.5	11.3 \pm 1.8	0.83	3.01	0.03	0.08	0.81	4.74	0.02	0.08
	9	4378 \pm 19	-20.0	-0.2 \pm 0.7	0.70	2.95	0.02	0.07	0.34	2.49	0.00	0.04
	10	4382 \pm 28	-20.3	-0.0 \pm 0.8	0.75	2.10	0.03	...	0.61	3.34	-0.10	-0.07
	14	4166 \pm 28	-19.9	-0.6 \pm 0.8	0.59	1.84	0.04	0.16	0.92	2.10	0.03	0.07
	16	4310 \pm 24	-19.4	-0.5 \pm 0.6	0.65	2.41	0.02	0.08	0.45	1.97	0.01	0.05
	18	4424 \pm 17	-19.5	-0.2 \pm 1.0	0.89	6.01	0.27	0.41	0.42	5.12	0.11	0.11
	19	4221 \pm 33	-19.3	0.6 \pm 1.9	0.86	1.30	0.02	0.06	0.65	1.24	0.01	0.04
	22	4871 \pm 26	-19.6	0.1 \pm 0.8	0.79	2.08	0.02	0.06	0.58	1.66	0.01	0.03
	25	4391 \pm 28	-18.9	-0.8 \pm 0.8	0.58	1.58	0.01	0.05	0.85	1.71	-0.00	0.04
	27	4196 \pm 17	-18.8	-0.4 \pm 0.7	0.56	1.07	0.02	0.04	0.90	1.16	0.02	0.05
	29	4238 \pm 34	-18.7	-0.1 \pm 1.3	0.81	1.92	0.01	0.03	0.66	1.56	0.01	0.02
	33	4076 \pm 30	-18.4	-0.5 \pm 0.9	0.80	0.91	0.01	0.03	0.81	0.89	0.00	0.01
	36	4829 \pm 36	-18.4	-0.1 \pm 1.0	0.47	1.46	0.01	0.04	0.44	1.26	0.00	0.01
	38	3962 \pm 33	-17.7	-0.7 \pm 0.7	0.25	1.21	0.01	0.01	0.27	1.31	0.00	0.00
	39	4316 \pm 34	-17.8	1.4 \pm 1.3	0.33	1.28	0.01	0.02	0.39	1.34	0.00	0.00
	41	4700 \pm 20	-17.5	48.1 \pm 5.3	0.30	2.15	0.09	0.10	0.21	1.87	0.07	0.07
	43	3964 \pm 34	-17.7	-0.3 \pm 0.6	0.71	1.67	0.04	0.07	0.68	1.82	0.05	0.05
	46	4731 \pm 34	-17.1	17.0 \pm 1.6	0.11	1.95	-0.00	0.05	0.10	1.78	0.01	0.01
	55	4655 \pm 50	-17.6	6.4 \pm 2.0	0.28	1.36	0.00	0.01	0.20	1.25	0.01	-0.00
	56	4849 \pm 42	-17.5	1.3 \pm 1.1	0.34	1.46	0.00	0.03	0.37	1.38	-0.00	0.02
	61	4695 \pm 37	-16.8	11.7 \pm 2.5	0.01	2.32	0.06	0.07	0.01	2.13	0.04	0.03
	62	4843 \pm 34	-17.4	-0.6 \pm 0.5	0.15	0.78	0.03	0.04	0.01	0.88	0.15	0.15
	66	4826 \pm 44	-17.5	1.3 \pm 1.3	0.51	1.06	0.04	0.05	0.36	0.82	0.01	0.02
	75	4397 \pm 119	-16.8	11.5 \pm 1.9	0.01	1.39	0.02	0.03	0.01	1.38	-0.01	0.01
	76	4963 \pm 35	-16.7	10.4 \pm 0.9	0.52	0.84	0.01	0.02	0.75	0.84	-0.01	-0.01
	89	4208 \pm 78	-16.6	6.6 \pm 2.4	0.20	0.90	0.09	0.13	0.55	1.28	0.02	0.01
	100	3917 \pm 102	-15.7	2.9 \pm 1.6	0.01	2.30	0.01	0.03	0.01	2.44	-0.02	-0.01
	109	4688 \pm 43	-16.1	36.5 \pm 8.3	0.29	1.46	0.02	0.03	0.43	1.64	0.01	-0.03
	111	3485 \pm 103	-16.2	3.7 \pm 3.0	0.01	0.56	0.02	0.04	0.02	0.68	0.00	0.02
	121	4235 \pm 103	-16.2	1.5 \pm 1.2	0.28	0.72	-0.00	0.01	0.52	0.73	0.01	0.00
	132	4285 \pm 75	-16.0	-2.4 \pm 2.6	0.51	0.62	0.01	0.01	0.43	0.77	0.00	0.01
	141	3722 \pm 44	-15.8	-1.8 \pm 0.8	0.20	0.73	-0.01	0.00	0.23	0.83	-0.00	-0.00
	150	4671 \pm 124	-16.3	-9.8 \pm 9.8	0.46	1.00	0.00	0.01	0.33	0.86	-0.02	-0.01
	158	3953 \pm 71	-15.9	1.0 \pm 1.2	0.13	0.93	0.01	0.02	0.34	1.03	-0.01	-0.01
	160	4228 \pm 63	-15.7	8.1 \pm 3.7	0.09	0.97	0.02	0.01	0.19	1.12	-0.01	0.00
N2563	1	4658 \pm 42	-21.1	1.8 \pm 1.6	0.94	6.28	0.01	0.04	0.88	6.80	0.02	0.04
	3	4857 \pm 45	-20.7	-0.0 \pm 1.0	1.00	3.95	0.01	0.11	0.82	3.79	0.02	0.12

Table 3—Continued

Field	ID	cz_0 (km s ⁻¹)	$M_R - 5\log h^a$	[OII] EW (Å)	cz_0				$cz = 9000$ km s ⁻¹			
					B/T ^b	$r_{1/2}^c$ (h ⁻¹ kpc)	R_A^d	R_T^e	B/T	$r_{1/2}$ (h ⁻¹ kpc)	R_A	R_T
N3557	5	4812±28	-20.6	0.7±0.9	0.68	4.45	0.03	0.16	0.49	3.61	0.01	0.06
	8	5267±30	-21.1	0.6±1.6	0.64	2.67	0.04	0.07	0.52	2.59	0.04	0.06
	9	4110±40	-18.4	3.8±0.7	0.02	3.00	0.06	-0.14	0.09	4.40	0.06	0.10
	10	5567±10	-20.2	18.6±3.4	0.54	5.19	0.15	0.24	0.52	5.10	0.09	0.15
	13	5148±24	-19.9	-0.3±0.8	0.91	2.20	0.02	0.06	0.84	1.75	0.04	0.06
	16	5346±68	-19.4	2.7±2.8	0.16	2.71	0.02	0.07	0.11	2.36	0.03	0.08
	18	4114±32	-18.9	2.6±0.8	0.07	3.84	0.04	0.17	0.03	4.42	0.03	0.13
	19	4529±29	-19.3	2.7±3.0	0.52	1.12	0.04	0.17	0.54	1.07	0.01	0.02
	21	4594±30	-19.2	-1.2±0.7	0.70	1.08	0.03	0.09	0.86	1.27	0.02	0.04
	23	4520±14	-18.6	11.9±1.4	0.01	2.42	0.10	0.11	0.00	2.44	0.07	0.08
	24	4914±10	-18.8	7.7±1.1	0.41	1.74	0.05	0.08	0.11	1.47	0.04	0.04
	27	5040±36	-18.7	1.8±0.7	0.13	5.65	0.03	0.11	0.05	4.78	0.02	-0.03
	28	5307±78	-18.8	2.3±1.6	0.10	3.33	0.02	0.06	0.04	2.97	0.02	0.03
	30	4674±27	-18.7	-0.2±0.6	0.81	1.76	0.01	0.03	0.70	1.84	0.01	0.05
	33	4270±24	-17.8	17.6±3.2	0.19	2.11	0.04	0.08	0.15	2.64	0.09	0.12
	34	4661±50	-18.6	-0.3±0.9	0.71	0.49	0.02	0.05	0.58	0.76	0.01	0.01
	35	5061±116	-18.2	5.8±8.5	0.08	2.23	0.02	0.08	0.00	1.91	0.04	0.05
	38	3945±31	-17.7	0.0±0.9	0.72	2.50	0.01	0.04	0.52	2.67	0.01	0.01
	40	4640±72	-18.0	5.7±2.9	0.10	1.68	0.01	0.04	0.17	1.80	0.00	0.02
	41	4917±25	-18.7	-0.1±0.6	0.54	1.25	0.01	0.04	0.59	0.90	0.01	0.03
	43	4473±80	-18.0	2.6±3.7	0.23	1.12	0.01	0.03	0.32	1.37	0.01	0.02
	44	4920±57	-17.8	-0.7±0.7	0.06	1.10	0.00	0.02	0.07	1.08	-0.00	-0.01
	50	4788±57	-17.7	5.3±4.2	1.00	1.62	0.01	0.06	0.71	1.33	0.00	0.02
	51	4606±73	-17.7	-1.1±1.2	0.68	0.60	0.00	-0.00	0.90	0.84	-0.01	0.05
	53	4286±39	-17.4	6.0±1.3	0.00	1.47	0.02	0.08	0.00	1.64	0.02	0.02
	58	4868±65	-17.5	2.8±10.2	0.36	1.76	0.01	0.05	0.21	1.77	-0.00	0.00
	82	5176±110	-17.3	8.8±3.2	0.77	1.11	0.01	0.03	0.56	0.92	0.00	0.01
	92	4504±45	-17.1	1.3±1.5	0.41	1.80	0.01	0.03	0.28	2.02	-0.00	0.05
	94	4844±37	-16.9	21.3±1.4	0.14	0.88	0.02	0.04	0.43	1.09	-0.01	0.00
	114	5076±87	-16.8	11.3±4.5	0.53	0.95	-0.01	0.01	0.80	1.30	-0.00	0.00
	120	4870±84	-16.7	3.5±2.3	0.58	1.10	0.01	0.03	0.53	1.17	-0.01	0.04
	148	4055±44	-16.1	-0.3±0.9	0.40	0.84	0.01	0.05	0.46	0.91	-0.01	-0.01
	150	4557±37	-16.2	41.9±5.3	0.01	1.28	0.02	0.08	0.03	1.41	0.01	0.07
	163	4375±77	-15.8	0.7±2.5	0.24	0.85	0.03	0.11	0.44	0.94	0.01	-0.00
	1	3009±27	-21.5	-0.2±0.7	0.75	5.54	0.04	-0.04	0.93	6.27	0.05	0.10
	5	2414±33	-18.9	7.0±0.8	0.46	5.71	0.16	...	0.14	13.44	-0.14	...
	6	3469±26	-19.6	-0.4±0.7	0.42	3.17	0.05	0.12	0.23	2.44	0.01	0.06
	7	3008±18	-20.2	-0.4±0.7	0.57	1.12	0.02	0.09	0.62	1.09	0.02	0.06
	9	2784±26	-20.2	-0.5±0.9	0.67	2.27	0.02	0.09	0.69	2.48	0.07	0.11
	11	2782±31	-17.7	-0.5±0.7	0.11	1.77	0.02	0.07	0.27	1.99	0.03	0.04
	16	3183±41	-16.5	15.8±1.7	0.04	2.00	-0.01	0.04	0.02	2.18	0.02	0.05
	19	3080±40	-16.8	1.5±1.6	0.14	1.16	0.01	0.03	0.64	1.74	-0.03	0.01
	25	2772±44	-15.8	8.8±2.0	0.00	1.42	0.02	0.07	0.01	1.30	0.01	0.01
	32	2623±65	-15.1	3.8±1.9	0.00	1.32	0.01	0.04	0.08	1.45	-0.00	0.06
	38	3062±71	-15.7	0.2±3.6	0.09	1.15	-0.00	0.02	0.15	1.34	-0.00	0.00
	47	3146±36	-15.8	47.2±1.5	0.57	0.44	0.04	0.06	0.63	0.37	-0.00	-0.00
	49	2640±68	-14.8	1.2±1.2	0.02	0.61	0.01	0.02	0.50	0.84	-0.03	0.03
	97	2751±102	-14.7	0.1±0.8	0.10	0.72	-0.00	0.01	0.55	0.86	0.04	-0.01
	106	3300±132	-14.6	-0.0±1.1	0.02	0.74	0.05	0.04	0.56	1.03	-0.07	-0.00
N4325	4	7564±41	-21.0	5.4±2.0	0.81	6.73	0.02	0.06	0.77	6.49	0.01	0.06
	7	7779±30	-20.8	3.3±1.4	0.79	2.96	0.08	0.15	0.46	2.54	0.14	0.29
	8	7941±27	-20.6	0.8±1.3	0.83	3.97	0.02	0.12	0.41	3.09	0.02	0.00
	11	7747±15	-19.8	4.9±1.4	0.10	3.31	0.04	0.09	0.08	2.95	0.03	0.07
	16	7661±36	-19.2	3.5±1.1	0.01	2.25	0.04	0.07	0.00	2.14	0.02	0.06
	17	7905±26	-19.2	0.9±1.0	0.25	1.68	0.03	0.06	0.27	1.57	0.01	0.04
	29	7187±23	-18.8	1.0±1.2	0.49	1.10	0.01	0.03	0.47	1.27	0.01	0.01
	30	7316±37	-18.8	21.7±0.7	0.40	0.93	0.04	0.07	0.46	0.95	0.01	0.02
	35	7397±60	-18.6	12.1±2.6	0.71	1.45	0.04	0.06	0.57	1.37	0.03	0.04
	37	7340±28	-18.5	-0.8±0.6	0.70	1.49	0.02	0.03	0.60	1.51	0.00	0.01
	50	7416±42	-18.1	1.8±1.8	0.51	0.73	0.01	0.03	0.63	0.84	0.00	0.01
	55	7018±49	-17.9	0.8±2.0	0.54	1.61	0.02	0.04	0.47	1.66	0.01	0.01
	60	7419±45	-18.0	22.4±2.7	0.00	1.82	0.10	0.15	0.00	1.80	0.04	0.09
	78	7650±67	-18.0	-9.7±-9.7	0.05	2.50	0.01	0.06	0.15	2.46	0.00	0.06
	79	7696±116	-18.0	4.6±1.2	0.12	2.01	0.02	0.05	0.17	2.03	0.00	0.00
	81	7707±80	-17.9	3.5±1.9	0.11	0.94	0.01	0.02	0.15	0.95	-0.00	0.00

Table 3—Continued

Field	ID	cz_0 (km s ⁻¹)	$M_R - 5\log h^a$	[OII] EW (Å)	cz_0				$cz = 9000$ km s ⁻¹			
					B/T ^b	$r_{1/2}^c$ (h ⁻¹ kpc)	R_A^d	R_T^e	B/T	$r_{1/2}$ (h ⁻¹ kpc)	R_A	R_T
N5129	83	7238±32	-17.6	12.6±0.9	0.35	0.98	0.03	0.04	0.33	1.04	0.01	0.03
	89	7972±62	-17.7	-0.3±1.1	0.63	1.24	0.03	0.05	0.39	1.02	0.00	0.02
	106	7647±38	-17.5	3.1±1.8	0.23	0.72	0.06	0.05	0.32	0.72	0.02	0.03
	129	7696±42	-17.1	0.7±1.1	0.48	1.01	0.01	0.03	0.47	1.13	-0.00	0.00
	133	7656±61	-17.5	5.0±2.1	0.64	1.02	0.01	0.02	0.63	1.01	0.00	0.01
	136	6978±41	-17.4	14.4±1.5	0.00	1.71	0.07	0.09	0.00	1.85	0.05	0.06
	137	6489±40	-16.8	23.4±1.1	0.34	0.99	0.01	0.04	0.35	1.14	0.01	-0.00
	1	6956±30	-21.9	1.7±1.7	0.90	9.10	0.02	0.05	0.89	9.03	0.04	0.09
	2	7285±25	-21.4	0.3±0.8	0.75	7.31	0.03	0.15	0.73	6.99	0.03	0.16
	4	6817±37	-20.8	1.6±0.9	0.88	4.32	0.02	0.04	0.77	4.00	0.02	0.07
	5	7239±14	-20.4	8.6±1.4	0.20	6.14	0.11	0.19	0.05	5.06	0.09	0.11
	6	6433±59	-19.8	3.9±1.3	0.05	4.92	0.07	...	0.07	10.16
	7	6839±25	-19.9	4.6±2.3	0.29	3.20	0.02	0.04	0.32	3.25	0.01	0.04
	8	7031±51	-19.7	1.8±1.8	0.10	4.78	0.03	0.07	0.02	4.54	0.03	0.08
	9	7273±35	-19.8	0.8±1.2	0.05	3.07	0.02	0.06	0.04	2.84	0.02	0.04
	10	6441±18	-19.4	8.9±1.3	0.06	3.34	0.05	0.08	0.04	3.60	0.05	0.07
	11	7451±48	-19.7	1.2±1.1	0.06	3.86	0.02	0.03	0.06	3.58	0.02	0.04
	12	6754±55	-19.5	3.5±1.1	0.41	1.96	0.03	0.06	0.48	2.16	0.02	0.03
	13	7157±37	-19.8	-1.4±1.1	0.98	1.63	0.02	0.04	1.00	1.55	0.02	0.05
	17	6768±81	-19.0	-0.4±0.7	0.48	2.52	0.03	0.04	0.46	2.43	0.03	0.03
	21	7061±32	-18.9	10.4±0.8	0.00	1.15	0.06	0.11	0.01	1.16	0.03	0.05
	30	7026±44	-18.5	2.2±1.3	0.37	1.42	0.01	0.01	0.49	1.38	0.02	0.01
	35	7105±70	-18.4	26.3±7.0	0.50	1.49	0.01	0.03	0.45	1.43	0.01	0.03
	38	7132±40	-18.4	3.6±1.7	0.14	1.37	0.01	0.02	0.18	1.35	0.01	0.01
	39	7393±35	-18.4	-0.7±0.6	0.80	2.50	-0.01	0.02	0.67	2.86	-0.00	0.01
	44	6905±36	-18.4	6.4±2.3	0.20	2.85	0.02	0.06	0.06	2.67	0.02	0.05
	52	7058±53	-18.5	6.1±1.6	0.13	2.59	0.05	0.07	0.06	2.47	0.03	0.04
	56	7261±72	-18.1	5.8±1.7	0.00	1.88	0.01	0.03	0.00	1.86	0.00	0.03
	58	6791±61	-18.3	5.9±1.4	0.19	2.65	0.02	0.15	0.29	2.84	0.03	0.13
	61	6890±55	-18.0	8.9±2.6	0.07	1.57	0.01	0.03	0.05	1.56	0.00	0.02
	62	7526±61	-18.4	2.6±0.9	0.30	2.31	-0.00	0.02	0.17	2.14	0.01	0.02
	83	7239±82	-18.0	6.1±1.5	0.00	2.04	-0.00	0.04	0.00	1.94	0.01	0.04
	95	7230±23	-17.5	20.6±2.6	0.00	2.67	0.04	0.10	0.00	2.52	0.03	0.07
	101	6233±45	-17.3	14.2±2.4	0.01	1.49	0.02	0.04	0.00	1.61	0.01	0.02
	102	6842±77	-17.4	2.0±1.3	0.24	1.47	0.02	0.02	0.27	1.44	-0.01	0.01
	107	7081±38	-17.5	0.8±1.0	0.66	1.14	0.02	0.03	0.75	1.12	0.01	0.02
	113	7387±71	-17.4	-1.7±1.4	0.75	0.89	0.00	0.02	0.84	0.93	0.01	0.02
	122	7060±66	-17.1	-0.3±1.4	0.26	1.61	0.01	0.03	0.23	1.61	0.00	0.01
	145	6760±40	-16.9	13.9±2.8	0.14	2.57	0.02	0.06	0.03	2.65	0.01	0.03
	159	7242±86	-17.2	2.5±2.2	0.03	0.97	0.01	0.03	0.01	0.94	-0.00	0.00
	9899	6701±39	-16.7	18.8±2.4	0.16	0.85	0.02	0.04	0.26	0.90	0.02	0.01

^a $H_0 = 100$ km s⁻¹Mpc⁻¹, $q_0 = 0.5$, flat cosmology

^bAverage error for B/T measurement is ~ 0.1 (Simard *et al.* 2000), although B/T can change by as much as 0.59 when the original (cz_0) and degraded ($cz = 9000$ km s⁻¹) values are compared for the individual galaxies.

^cAverage error for $r_{1/2}$ is $\sim 10\%$ (Simard *et al.* 2000).

^dAverage random error for R_A is ~ 0.02 (Simard *et al.* 2000; Im *et al.* 2000), although R_A can change by as much as 0.16 when the original (cz_0) and degraded ($cz = 9000$ km s⁻¹) values are compared.

^eAverage random error for R_T is ~ 0.02 (Simard *et al.* 2000; Im *et al.* 2000), although R_T can change by as much as 0.30 when the original (cz_0) and degraded ($cz = 9000$ km s⁻¹) values are compared.

Table 4. Global Group Characteristics

Group	\bar{v}	z_0		$cz = 9000 \text{ km s}^{-1}$	
		(Early Types) $_T^a$	(Early Types) $_I^b$	(Early Types) $_T$	(Early Types) $_I$
HCG 42	3830 \pm 47	15/25 (60%)	12/19 (63%)	15/25 (60%)	13/19 (68%)
HCG 62	4356 \pm 50	21/38 (55%)	15/25 (60%)	21/38 (55%)	15/25 (60%)
NGC2563	4775 \pm 65	20/36 (56%)	14/20 (70%)	20/36 (56%)	12/20 (60%)
NGC3557	2843 \pm 64	6/15 (40%)	5/12 (42%)	8/15 (53%)	7/12 (58%)
NGC4325	7558 \pm 70	12/23 (52%)	8/11 (73%)	11/23 (48%)	7/11 (64%)
NGC5129	6998 \pm 51	10/34 (29%)	8/19 (42%)	11/34 (32%)	8/19 (42%)
<i>Average</i>		84/171 (49%)	62/106 (58%)	86/171 (50%)	62/106 (58%)

^aThe subscript T denotes all group members in the $1^\circ \times 1^\circ$ field.

^bThe subscript I denotes only group members within $R \leq 0.25h^{-1} \text{ Mpc}$ ($H_0 = 100h \text{ km s}^{-1}\text{Mpc}^{-1}$; $q_0 = 0.5$) of the group's center.

Fig. 1.— *1a*: Thumbnails of all the galaxies in our sample (189) at their observed redshift. The pixel area in each thumbnail is 12 times the galaxy’s isophotal area as defined by SExtractor. Reference numbers and absolute magnitudes corresponding to Table 3 are listed in the bottom and upper left corners respectively. In these images, the seeing ranges from 1.''3 to 2.''6. *1b*: The best-fit de Vaucouleurs bulge with exponential disk models for the same galaxies found by GIM2D. The bulge fraction is listed in the upper left corner. *1c*: The residual images created by subtracting the best GIM2D model from the original galaxy image. In the upper left corner, the asymmetry parameter and total fraction of residual light are shown (R_A, R_T).

Fig. 2.— The same scheme as in Fig. 1 but now for the redshifted ($cz = 9000 \text{ km s}^{-1}$) galaxies. The effective resolution for all the galaxies is now $0.87h^{-1} \text{ kpc}$.

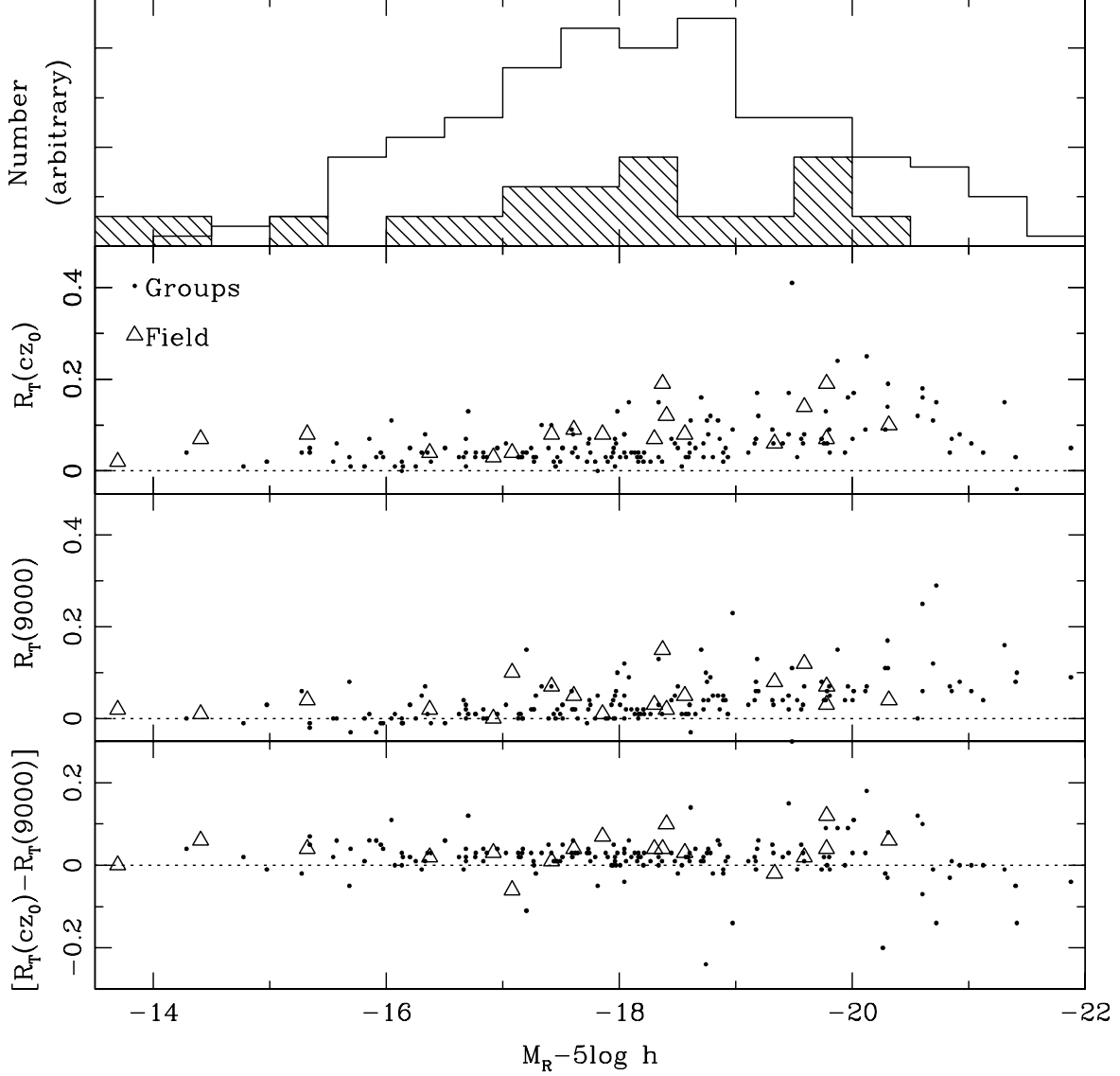


Fig. 3.— *Top Panel:* Absolute magnitude distribution of group (open bins) and field (hatched bins) samples; the field sample is scaled arbitrarily by a factor of three to make comparison of the samples easier. Both samples roughly cover the same absolute magnitude range, and a Kolmogorov-Smirnov test finds the two distributions are indistinguishable at the 95% confidence level. *Middle Panels:* The total fraction of residual light (R_T) as a function of absolute magnitude (M_R) at the observed (cz_0) and common ($cz = 9000 \text{ km s}^{-1}$) redshift. Field galaxies are shown as open triangles and group galaxies as filled circles. *Bottom Panel:* The difference between the total residuals, $[R_T(cz_0) - R_T(9000)]$. For galaxies fainter than $M_R = -20 + 5 \log h$, the fits “improve” slightly (0.02 ± 0.01) after they are redshifted to $cz = 9000 \text{ km s}^{-1}$.

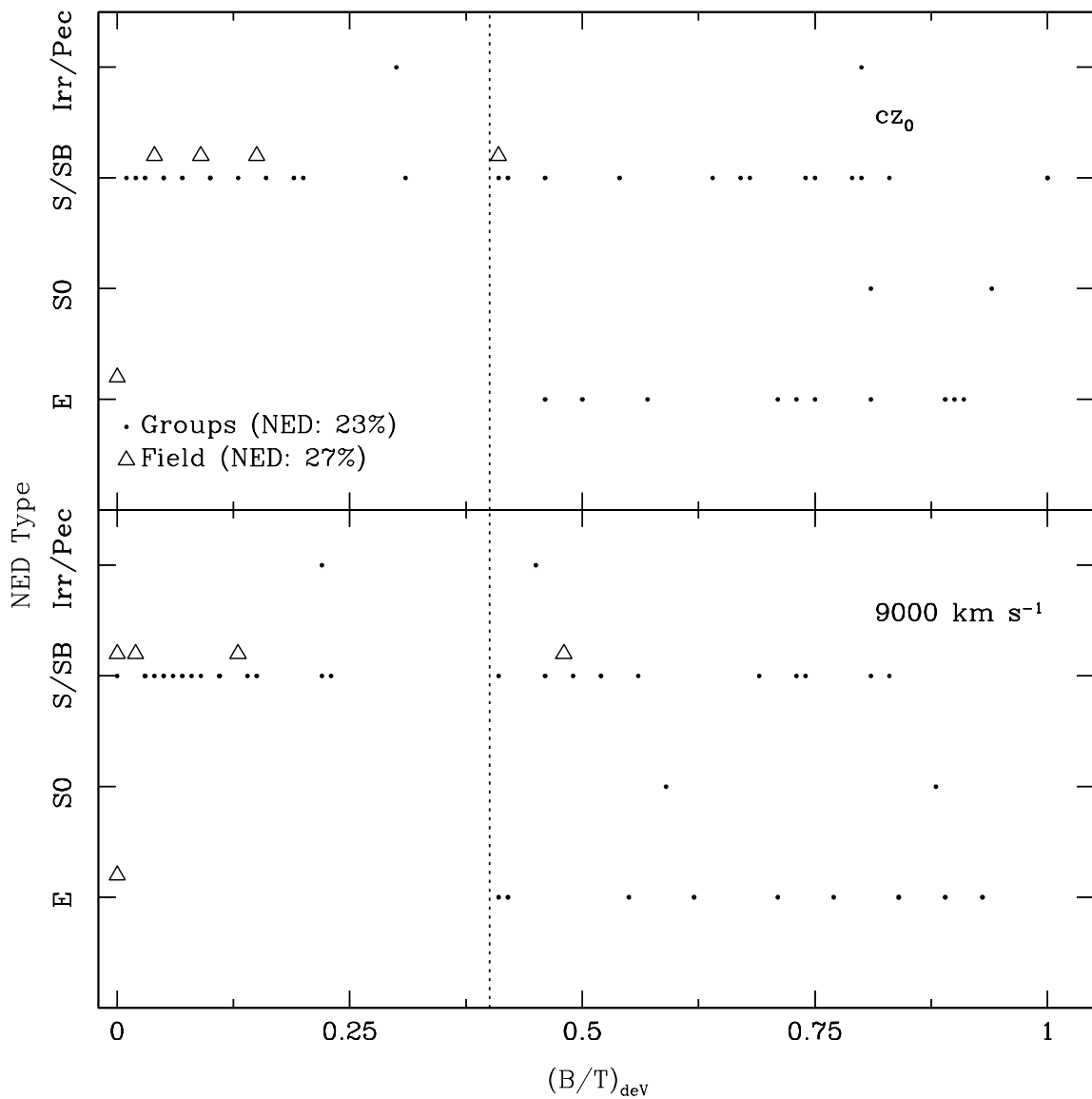


Fig. 4.— Comparison of measured B/T to published morphological type. We split the morphological types into four bins: Ellipticals, S0’s, Spirals/Barred Spirals, and Irregulars/Peculiars. The upper panels correspond to the measured B/T for each galaxy at its observed redshift for the group and field. The field points are offset slightly in the y-direction for clarity. Only a small set of galaxies ($\sim 24\%$) in our sample have been morphologically classified in the literature. Comparing type to our measured B/T , we define “early-type” galaxies to have $B/T \geq 0.4$.

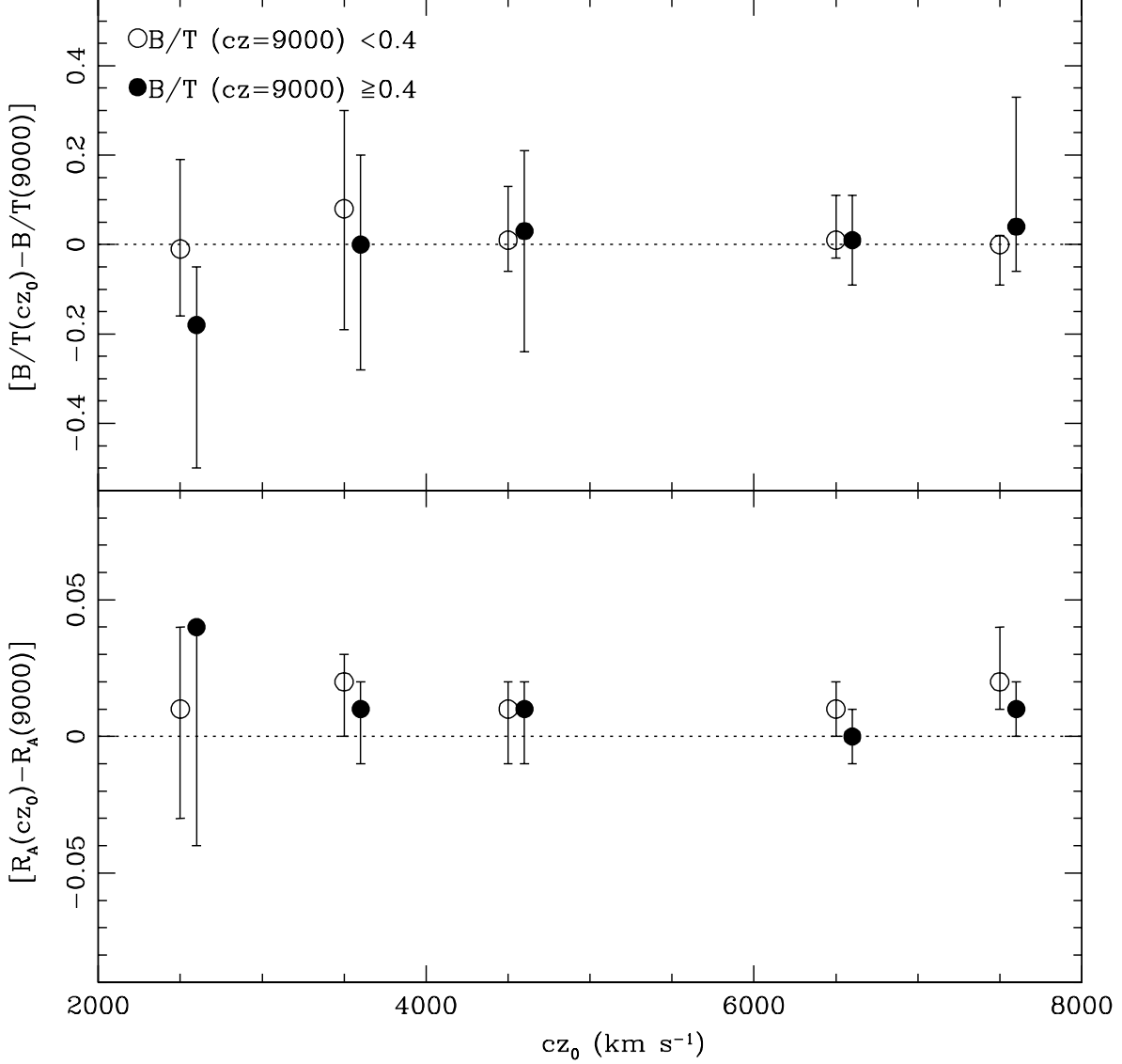


Fig. 5.— *Top Panel:* The median change in B/T when the group galaxies are moved from cz_0 to $cz = 9000 \text{ km s}^{-1}$ and binned to the same effective resolution ($0.87h^{-1} \text{ kpc}$). The redshift bins are 1000 km s^{-1} wide, and we use the group’s (not the galaxy’s) redshift. The open circles are for galaxies with $(B/T)_{cz9000} < 0.4$ and the filled circles for galaxies with $(B/T)_{cz9000} \geq 0.4$; the two points in each bin are offset slightly in the x-direction for clarity. The asymmetric errorbars correspond to 1σ in the $[(B/T)_{cz_0} - (B/T)_{cz9000}]$ distribution about the median; lack of an errorbar indicates clumping at that value. Although galaxies have been redshifted by up to a factor of four and the effective resolution degraded by as much as a factor of five, the median change in B/T is consistent with zero for both morphological bins. *Bottom Panel:* Same as above except for the asymmetry parameter R_A . Comparing the results for the original and redshifted galaxies, we observe a slight decrease in the ability to recover asymmetric features with decreased effective resolution (0.02 ± 0.01).

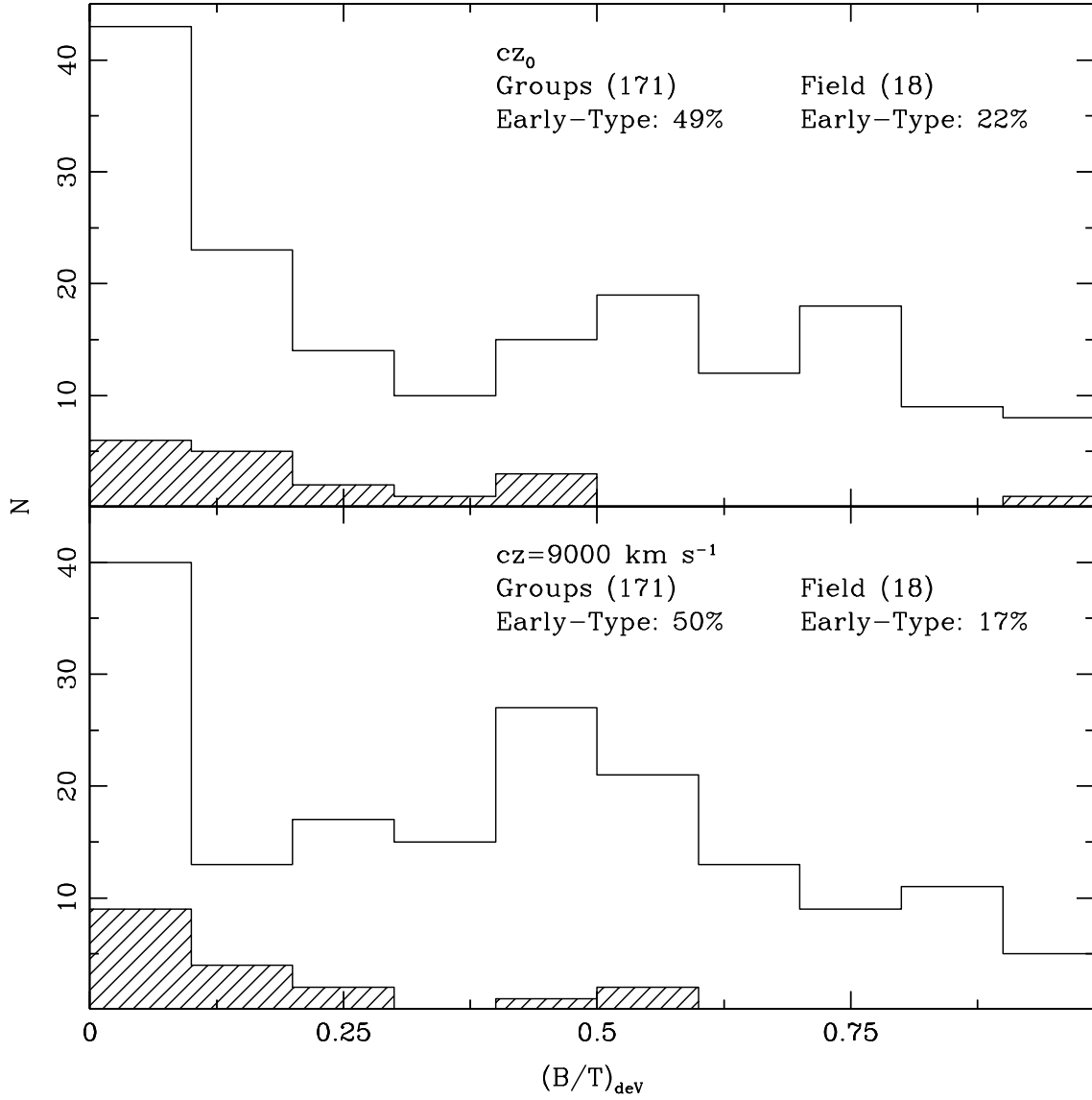


Fig. 6.— Histogram of B/T measured with GIM2D using a 2D profile with a de Vaucouleurs bulge and exponential disk. The bin size is 0.1. The upper panels correspond to B/T measured at the observed redshift and the lower panels to B/T measured at $cz = 9000 \text{ km s}^{-1}$. The groups are the open bins and the field the hatched bins. A K-S test comparing the group and field distributions at their observed redshifts and at $cz = 9000 \text{ km s}^{-1}$ rule out a common parent distribution with $> 95\%$ certainty in both cases.

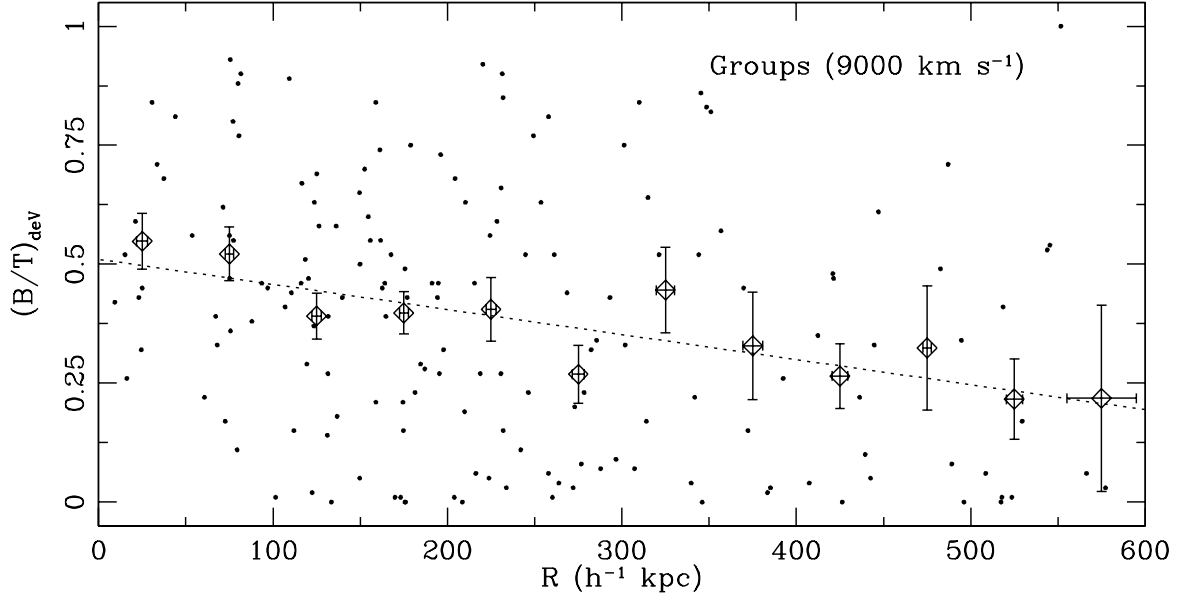


Fig. 7.— B/T as function of distance from group center for all group galaxies (171) at $cz = 9000 \text{ km s}^{-1}$ and within $R < 0.5h^{-1} \text{ Mpc}$, approximately the group virial radius. The open diamonds represent the average B/T for each $50h^{-1} \text{ kpc}$ bin. The errorbars correspond to the standard error of the mean in the R and B/T distributions for each bin. There is a significant trend of decreasing B/T with increasing radius ($> 95\%$ significant using the Spearman rank test). The dotted line is the least-squares fit to the data. Despite their small number of members, these X-ray detected, poor galaxy groups display a morphology-radius (\sim density) relationship similar to that of galaxy clusters.

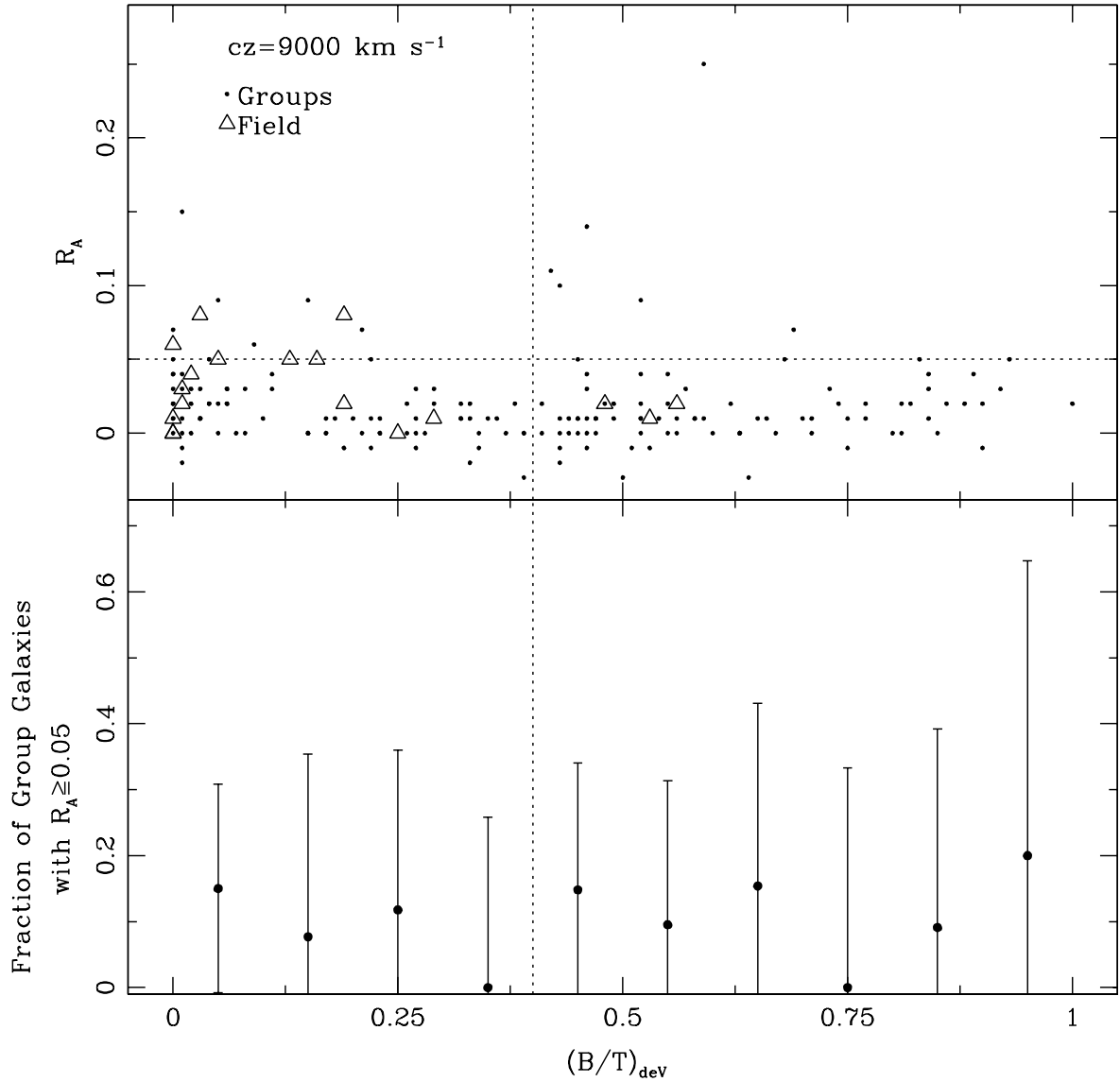


Fig. 8.— Distribution of the asymmetry parameter R_A with respect to B/T for the group and field populations at $cz = 9000 \text{ km s}^{-1}$. *Top Panel:* R_A as a function of B/T . Group members are the filled circles and the field are the open triangles. The dotted lines represent $R_A = 0.05$ and $B/T = 0.4$, the defined lower limits for asymmetric and bulge-dominated galaxies respectively. *Bottom Panel:* Fraction of group galaxies with significant galaxy asymmetry ($R_A \geq 0.05$) versus B/T ; 1σ errorbars are shown for each bin. There is no significant correlation of B/T with either R_A or the fraction of galaxies with high R_A .

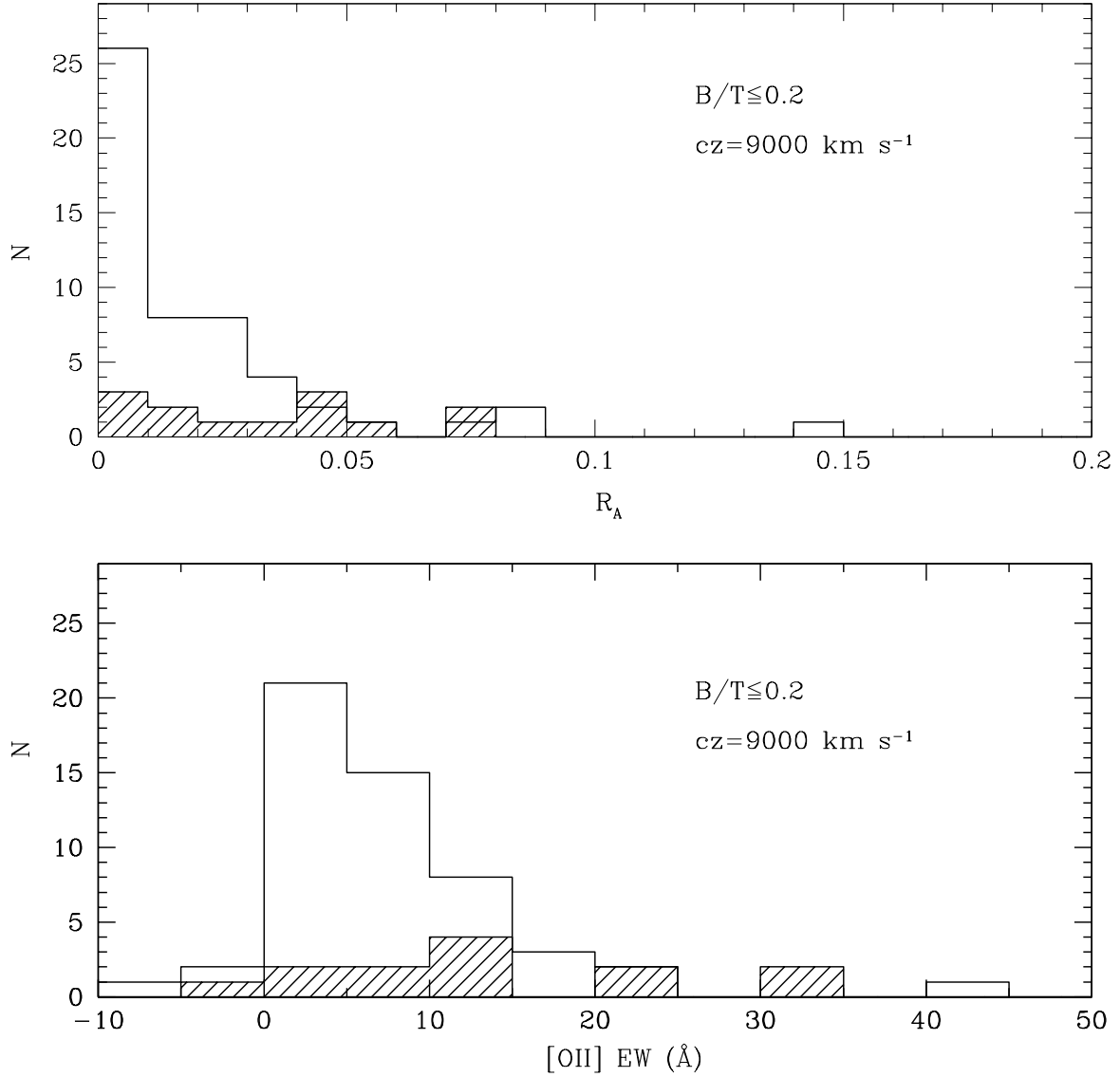


Fig. 9.— *Top Panel:* R_A distribution for the most disk-dominated ($B/T < 0.2$) group (open bins) and field (hatched bins) galaxies. *Bottom Panel:* $[\text{OII}] \text{ EW}$ distribution for the same group and field galaxies. In both panels, a K-S test rules out a common distribution between group and field galaxies with $> 95\%$ certainty.

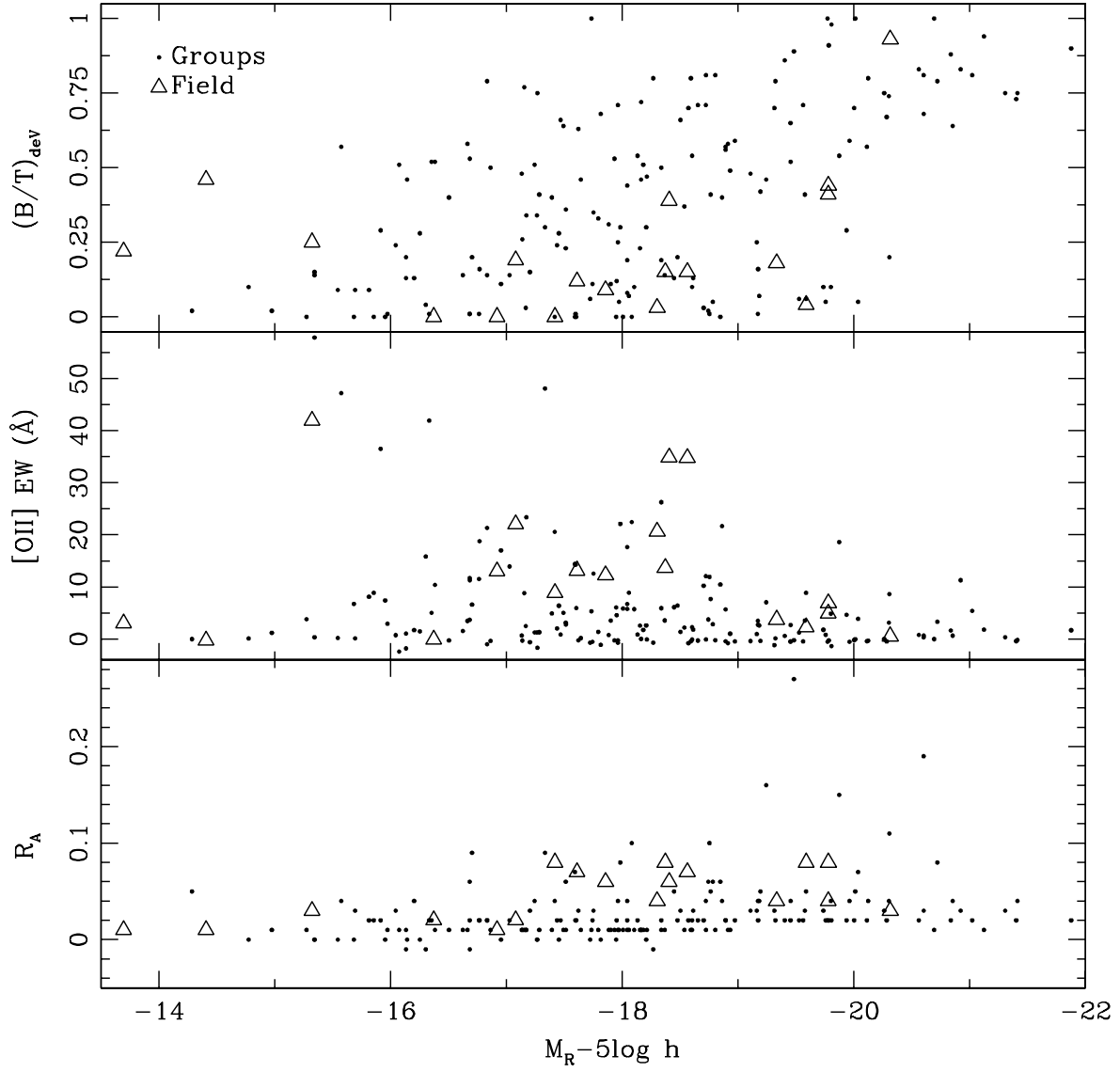


Fig. 10.— Distribution of B/T , $[\text{OII}]$ equivalent width, and asymmetry R_A versus absolute magnitude (M_R) for group and field galaxies shown in the top, middle, and bottom panel, respectively. Despite having similar M_R ranges, the group and field galaxy populations differ in their B/T , $[\text{OII}]$ EW, and R_A distributions.

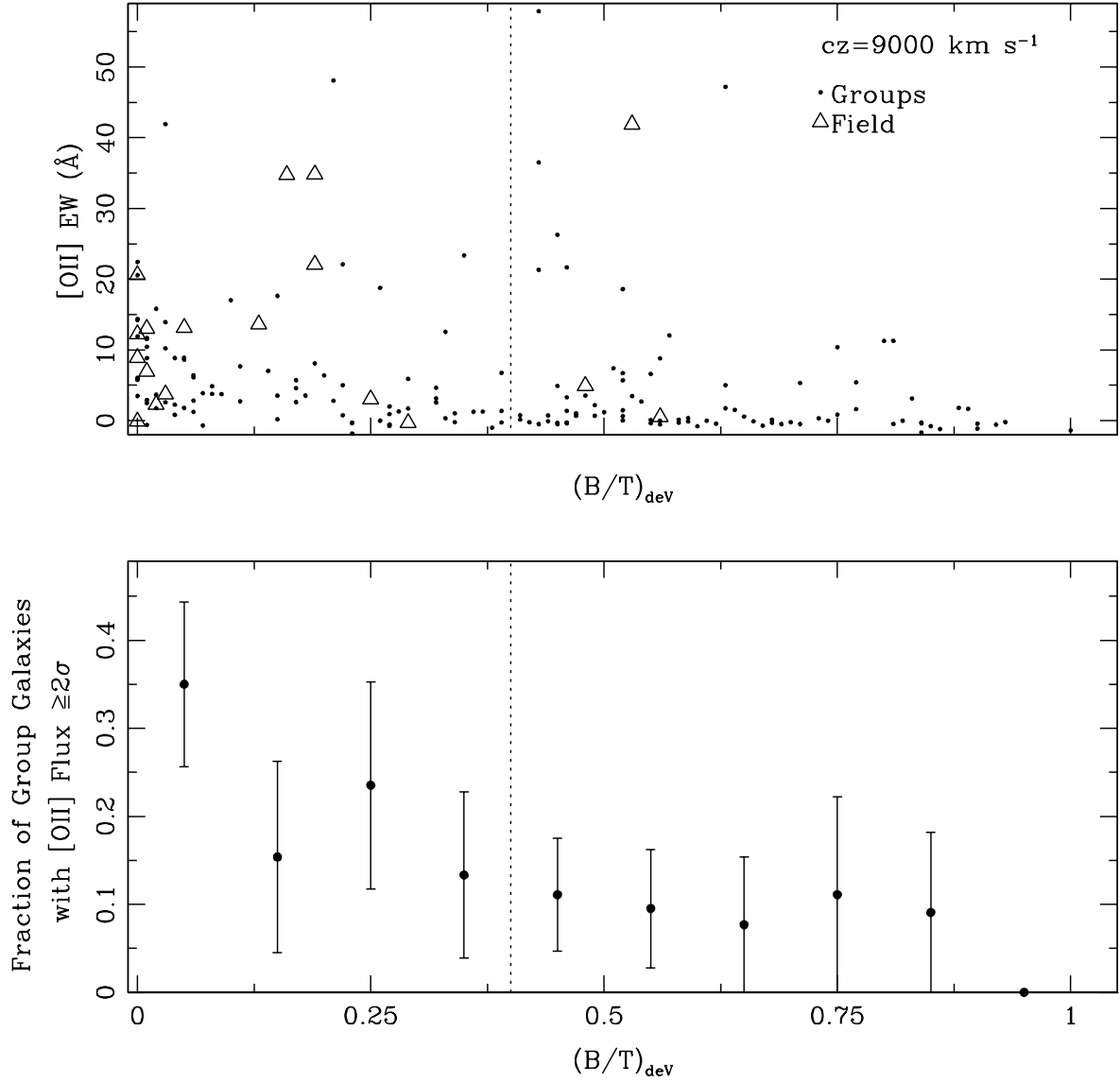


Fig. 11.— Distribution of [OII] emission with respect to B/T for the groups and the field at $cz = 9000 \text{ km s}^{-1}$. *Top Panel:* The [OII] equivalent width versus B/T . The dotted line represents $B/T = 0.4$, the defined lower limit for bulge-dominated galaxies. *Bottom Panel:* Fraction of group galaxies with [OII] flux greater than 2σ versus B/T , where σ is the error in the flux; 68% confidence errorbars are shown for each bin. The fraction of galaxies with significant [OII] flux drops by almost two beyond $B/T \sim 0.3$.

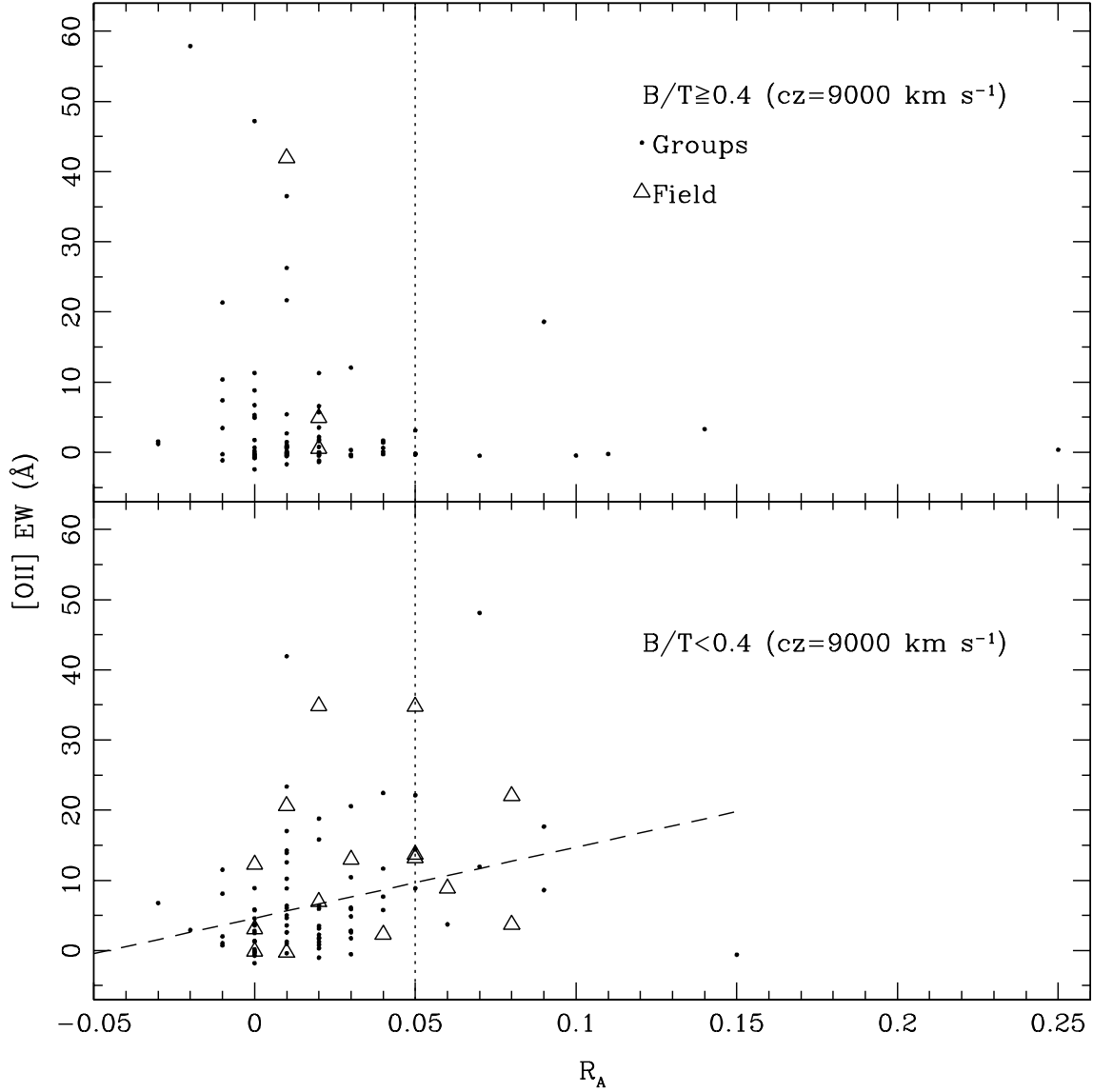


Fig. 12.— Distribution of [OII] emission with respect to the asymmetry parameter R_A for the groups and the field. *Top Panel:* The [OII] equivalent width versus R_A for early-type galaxies ($B/T \geq 0.4$). The dotted line represents $R_A = 0.05$, the defined lower limit for asymmetric galaxies. *Bottom Panel:* The same except for late-type galaxies ($B/T < 0.4$). There is a correlation between R_A and [OII] EW for $B/T < 0.4$ group galaxies; the least-squares fit to only the group members is represented by the dashed line in the $B/T < 0.4$ panel. The trend is $> 95\%$ significant using the Spearman rank test.

This figure "smfig1a.jpg" is available in "jpg" format from:

<http://arxiv.org/ps/astro-ph/0010278v1>

This figure "smfig1b.jpg" is available in "jpg" format from:

<http://arxiv.org/ps/astro-ph/0010278v1>

This figure "smfig1c.jpg" is available in "jpg" format from:

<http://arxiv.org/ps/astro-ph/0010278v1>

This figure "smfig2a.jpg" is available in "jpg" format from:

<http://arxiv.org/ps/astro-ph/0010278v1>

This figure "smfig2b.jpg" is available in "jpg" format from:

<http://arxiv.org/ps/astro-ph/0010278v1>

This figure "smfig2c.jpg" is available in "jpg" format from:

<http://arxiv.org/ps/astro-ph/0010278v1>